Heat-transport enhancement in rotating turbulent Rayleigh-Bénard convection

Stephan Weiss, Ping Wei, and Guenter Ahlers

Heat-transport enhancement in rotating turbulent Rayleigh-Bénard convection

Stephan Weiss[1,2], Ping Wei[1], and Guenter Ahlers[1]

[1]*Department of Physics, University of California, Santa Barbara, CA 93106, USA and*
[2]*Max Planck Institute for Dynamics and Self-Organization (MPIDS), 37077 Göttingen, Germany*

We present new Nusselt-number (Nu) measurements for slowly-rotating turbulent thermal convection in cylindrical samples with aspect ratio $\Gamma = 1.00$ and provide a comprehensive correlation of all available data for that Γ. In the experiment compressed gasses (nitrogen and sulfur hexafluoride) as well as the fluorocarbon C_6F_{14} (3M Fluorinert$^{\text{TM}}$ FC72) and Isopropanol were used as the convecting fluids. The data span the Prandtl-number (Pr) range $0.74 < \text{Pr} < 35.5$ and are for Rayleigh numbers (Ra) from 3×10^8 to 4×10^{11}. The relative heat transport $\text{Nu}_r(1/\text{Ro}) \equiv \text{Nu}(1/\text{Ro})/\text{Nu}(0)$ as a function of the dimensionless inverse Rossby number $1/\text{Ro}$ at constant Ra is reported. For $\text{Pr} \approx 0.74$ and the smallest $\text{Ra} = 3.6 \times 10^8$ the maximum enhancement $\text{Nu}_{r,max} - 1$ due to rotation is about 0.02. With increasing Ra, $\text{Nu}_{r,max} - 1$ decreased further, and for $\text{Ra} \gtrsim 2 \times 10^9$ heat-transport enhancement was no longer observed. For larger Pr the dependence of Nu_r on $1/\text{Ro}$ is qualitatively similar for all Pr. As noted before, there is a very small increase of Nu_r for small $1/\text{Ro}$, followed by a decrease by a percent or so, before, at a critical value $1/\text{Ro}_c$, a sharp transition to enhancement by Ekman pumping takes place. While the data revealed no dependence of $1/\text{Ro}_c$ on Ra, $1/\text{Ro}_c$ decreased with increasing Pr. This dependence could be described by a power law with an exponent $\alpha \simeq -0.41$. Power-law dependences on Pr and Ra could be used to describe the slope $S_{\text{Ro}}^+ = \partial \text{Nu}_r/\partial(1/\text{Ro})$ just above $1/\text{Ro}_c$. The Pr and Ra exponents were $\beta_1 = -0.16 \pm 0.08$ and $\beta_2 = -0.04 \pm 0.06$ respectively. Further increase of $1/\text{Ro}$ led to further increase of Nu_r until it reached a maximum value $\text{Nu}_{r,max}$. Beyond the maximum, the Taylor-Proudman (TP) effect, which is expected to lead to reduced vertical fluid transport in the bulk region, lowered Nu_r. $\text{Nu}_{r,max}$ was largest for the largest Pr. For $\text{Pr} = 28.9$, for example, we measured an increase of the heat transport by up to 40% ($\text{Nu}_r - 1 = 0.40$) for the smallest $\text{Ra} = 2.2 \times 10^9$, even though we were unable to reach $\text{Nu}_{r,max}$ over the accessible $1/\text{Ro}$ range. Both $\text{Nu}_{r,max}(\text{Pr}, \text{Ra})$ and its location $1/\text{Ro}_{max}(\text{Pr}, \text{Ra})$ along the $1/\text{Ro}$ axis increased with Pr and decreased with Ra. Although both could be given by power-law representations, the uncertainties of the exponents are relatively large.

I. INTRODUCTION

In addition to being of major fundamental interest in fluid mechanics, thermal convection in a rotating reference frame has been a topic of research for many years because it occurs in many geo- and astro-physical systems. Important examples occurring in nature include atmospheric flows in solar planets [see, for instance, Ref. [1]], convection in an outer portion of the sun [2] which determines the temperature on Earth, and the flow of conducting material in Earth's outer core which generates the magnetic field that protects us from cosmic radiation [3].

Studies of thermal convection in the laboratory or in numerical simulations use or consider a fluid which is confined by a cold horizontal plate from above and a parallel warm plate from below. This system is known as Rayleigh-Bénard convection or RBC [for a general introduction to RBC, see for instance [4, 5]; for more detailed reviews see *e.g.* [6–8] and references therein]. The vertical temperature difference across the sample is expressed in dimensionless form by the Rayleigh number Ra (see Eq. 3 below). For sufficiently large Ra the fluid flow is turbulent [9–13] and the heat transport, expressed in dimensionless form as the Nusselt number Nu (see Eq. 8 below), is strongly enhanced by the fluid motion. In this case, most of the temperature drop across the sample takes place within two thin thermal boundary layers (BLs), one below the top and the other above the bottom plate [14–17], while the temperature in the bulk of the sample, even though vigorously fluctuating, remains nearly constant in the time average (see, however, Refs. [18–22] for more detailed descriptions). In the bulk there are large-scale flow structures (the "large-scale circulation" or LSC) in addition to the fluctuations on a wide range of smaller scales [23]. In the case of a sample with height L close to its diameter D the LSC takes the form of a single convection roll with up flow and down flow along the side wall on opposite sides. The LSC has a dynamic characteristic of a stochastically driven system [24, 25]. The circulation plane of the LSC diffuses azimuthally, driven by the small-scale fluctuations. The LSC amplitude varies irregularly in time, and occasionally undergoes a cessation where it briefly vanishes completely. All the work discussed in the present paper is about turbulent convection in a cylindrical sample with aspect ratio $\Gamma \equiv D/L = 1.00$.

Rotating a sample of turbulent RBC about its vertical axis at an angular frequency Ω introduces a host of interesting new phenomena (for a recent review, see [26]). In dimensionless form Ω is usually expressed by the inverse Rossby number $1/\text{Ro}$ (see Eq. 6) or the inverse Ekman number $1/\text{Ek}$ (see Eq. 7), both of which are proportional to Ω. Constant rotation affects the flow field, and thus Nu, because it couples to the velocity and thereby introduces the Coriolis force. It also introduces a centripetal force, but this is often neglected in a theoretical analysis

and experiments tend to be designed so as to minimize its influence.

Rotation stabilizes the pure conduction state and thus leads to an increase of the critical Rayleigh number $Ra_c(\Omega)$ for the onset of convection [27–32]. For somewhat larger Ra this stabilizing influence is reflected in a reduction of the heat flux when the rotation rate is increased at constant $Ra > Ra_c$. However, when Ra is large enough for the convection to be turbulent, slow rotation (small $1/Ro$ or $1/Ek$) at constant Ra leads to an *enhanced* Nu [29, 30, 33]. We shall describe this phenomenon in terms of the relative Nusselt number

$$Nu_r = Nu(1/Ro)/Nu(0) . \qquad (1)$$

It is believed that this enhancement is due to Ekman pumping that occurs when thermal plumes that emerge from the thermal boundary layers are turned into vortices by the Coriolis force; these vortices pump hot or cold fluid from the bottom or top boundary layers into the bulk regions [29].

A remarkable recent experimental discovery was that the heat-flux enhancement does not occur for arbitrarily small rotation rates. Rather, $1/Ro$ has to exceed a critical value $1/Ro_c$ before Ekman pumping sets in [34]. At $1/Ro_c$ there is a transition between two different turbulent states, one without and the other with Ekman vortices. The value for $1/Ro_c$ depends on Γ and the experimental data suggest that it vanishes as Γ tends toward infinity, thus leaving the unbounded state without this transition [34, 35]. A Ginzburg-Landau like model was developed that explains the transition as a result of the influence of the lateral boundaries on the vortex formation inside the fluid [36, 37]. In this model, the transition is a forward bifurcation, causing a discontinuity of the slope

$$S_{Ro} = [\partial Nu_r/\partial(1/Ro)] \qquad (2)$$

at $1/Ro_c$.

Above $1/Ro_c$ the heat transport first increases linearly with $1/Ro$, but as $1/Ro$ becomes larger S_{Ro} decreases and eventually becomes negative, thus leading to a maximum of $Nu_r(1/Ro)$ at constant Ra and Pr. Qualitatively this phenomenon is due to a competition between Ekman pumping (which enhances Nu) and the stabilizing influence due to the Taylor-Proudman (TP) effect (see *e.g.* Ref. [38]) which tends to suppress vertical velocity gradients and thereby introduces temperature gradients in the bulk and reduces Nu. The state of the system in the parameter range where $Nu_r > 1$ because Ekman pumping is more effective than TP suppression often is referred to as *buoyancy-driven turbulence.* The current investigation focusses on this parameter range.

It had been thought that above $1/Ro_c$ $Nu_r(1/Ro)$ at constant Ra evolves smoothly with increasing $1/Ro$ in the buoyancy-driven regime without any further transitions. However, recently it was discovered [39] that there actually is a *sequence* of transitions where S_{Ro} changes

discontinuously while, within the resolution of the experiment, Nu_r remains continuous. Between these transitions Nu_r is well approximated by a linear dependence on $1/Ro$. For modest Ra the slope changes at the transitions are not very large and were not easily recognized in the data; but at $Ra = \mathcal{O}(10^{11})$ and larger the transitions became quite obvious. For the analysis of the present paper we shall not take the transitions beyond $1/Ro_c$ into consideration and focus only on the dependence on Ra and Pr of $1/Ro_c$, of the slopes S_{Ro}^- and S_{Ro}^+ immediately below and above $1/Ro_c$, and of the height $Nu_{r,max}$ and location $1/Ro_{max}$ along the $1/Ro$ axis of the maximum of Nu_r.

With further increase of $1/Ro$ the system enters a *rotation-dominated* regime where the TP suppression of the heat transport is larger than the Ekman-pumping enhancement (*i.e.* $Nu_r < 1$) [see *e.g.* Refs. [29–31, 33, 40–42]]. When $1/Ro$ becomes even larger (but Ra is large enough for the system to remain in a turbulent state), one finds the so-called geostrophic flow regime where Nu_r is diminished to values well below one and where the Coriolis force is balanced by pressure gradients [see *e.g.* Refs. [41–44]]. While this regime is of exceptional interest in geophysics, astrophysics, atmospheric science, and oceanography, it is difficult to reach experimentally and beyond the scope of the present paper.

There is no uncertainty about the existence of the above-mentioned regimes; but many details are still unclear, as for example the influence of Pr on the heat-transport enhancement at small $1/Ro$. Here we consider large Ra and small rotation rates and investigate the heat-transport enhancement in this buoyancy-driven regime. A great deal of work already had been done on this problem using experiments (*e.g.* Refs. [37, 45–50]) and direct numerical simulations (DNS) (*e.g.* Refs. [34, 51, 52]); our measurements add to the understanding of the Pr and Ra dependences of the observed phenomena. Our analysis of all the available data for $\Gamma = 1.00$ provides a unified interpretation.

We found that $1/Ro_c$ is, within the uncertainty of the data, independent of Ra and decreases with increasing Pr. This Pr dependence can be described by the power law $1/Ro_c \propto Pr^\alpha$ with $\alpha \simeq -0.41$. The slope S_{Ro}^- of Nu_r just below $1/Ro_c$ is negative and has a tendency to become more so with increasing Ra, but the data are not good enough to warrant a description in terms of a power law. The initial slope S_{Ro}^+ immediately above $1/Ro_c$ is positive and decreases slightly with increasing Pr and Ra. The data can be represented well by a power law of the form $S_{Ro}^+ \propto Pr^{-0.16} \cdot Ra^{-0.04}$. The maximum heat-transport enhancement $Nu_{r,max}$ decreases with increasing Ra at constant Pr, and the decrease can be described by the power law $Nu_{r,max} \propto Ra^{\delta_2}$ with $\delta_2 = -0.35$. With increasing Pr at constant Ra $Nu_{r,max}$ increases. Although the data are not so definitive, we assumed also for the Pr-dependence a power law $Nu_{r,max} \propto Pr^{\delta_1}$, but the fitted exponent value $\delta_1 \approx 0.65$ is subject to a large

uncertainty. For Pr = 28.9 and Ra = 2.2×10^9 we measured an increase of the heat transport by as much as 40%, even though our accessible range of 1/Ro was not sufficient to actually reach the maximum. In contrast, for Pr= 0.74 the heat transport increased by not more than 2% for the smallest Ra, and no enhancement could be measured for larger Ra.

In the next section we define the relevant dimensionless parameters needed to describe this system. After that, in Sec. III, we describe the general features of the heat-transport enhancement by using previous measurements taken with water (Pr = 4.38) and published in Ref. [47]. We then briefly describe the experimental apparatus in section IV. Section V presents measurement results and data analysis. The paper ends with a summary and discussion where we present our present understanding of the observed phenomena in the weakly rotating regime.

II. RELEVANT PARAMETERS

Investigating thermal convection is usually done in cylindrical vessels of diameter D and height L that are terminated by a warm plate of temperature T_b from the bottom and a colder plate at temperature T_t from above. If the temperature difference $\Delta T = T_b - T_t$ is sufficiently small, fluid properties can be assumed to be constant throughout the cell and the system is described by the Boussinesq equations [53–55]. In these equations, two dimensionless control parameters occur. They are the Rayleigh number

$$\mathrm{Ra} = \frac{\alpha g \Delta T L^3}{\nu \kappa} \qquad (3)$$

and the Prandtl number

$$\mathrm{Pr} = \frac{\nu}{\kappa}. \qquad (4)$$

Here α, κ and ν denote the isobaric thermal expansion coefficient, the thermal diffusivity, and the kinematic viscosity of the fluid. These properties are evaluated at the mean temperature $T_m = (T_b + T_t)/2$. The gravitational acceleration is g. For a cylindrical sample a third relevant parameter is the aspect ratio

$$\Gamma \equiv D/L. \qquad (5)$$

The value of Ra for which the flow becomes turbulent depends on Pr. An increase of Pr stabilizes the flow, *i.e.* the transition to turbulence is shifted to larger values of Ra [9–11, 13]. All measurements considered in this paper, including those at the larger Pr values, are done in the fully turbulent regime.

From the definitions of Ra and Pr we see that the first measures the thermal driving of the flow (*i.e.*, the ratio between the buoyancy and the damping forces), while the second indicates whether thermal diffusion or viscosity is the main reason for the damping of the flow.

When the sample rotates around its vertical axis, the angular rotation frequency Ω (in rad/s) is an additional control parameter that can be varied. There are several dimensionless parameters that can be used in the governing equations to express the effect of Ω. Here we shall use the Rossby number

$$\mathrm{Ro} = \frac{\sqrt{\alpha g \Delta T / L}}{2\Omega}, \qquad (6)$$

which describes the ratio between the buoyant and Coriolis forces and the Ekman number

$$\mathrm{Ek} = \frac{\nu}{\Omega L^2} = 2\mathrm{Ro} \cdot \sqrt{\frac{\mathrm{Pr}}{\mathrm{Ra}}} \qquad (7)$$

which compares the viscous with the Coriolis force. While either of these two numbers is sufficient to describe the system, one or the other may be more appropriate depending on parameter values and issues of interest. Following the convention of recent previous publications, we shall use the inverse Rossby number 1/Ro and the inverse Ekman number 1/Ek because these are proportional to Ω.

An important global property usually investigated is the heat flux from the bottom to the top plate as expressed by the dimensionless Nusselt number

$$\mathrm{Nu} = \frac{QL}{A\lambda \Delta T}. \qquad (8)$$

This quantity relates the overall heat-current density Q/A to the purely conductive heat flux $\lambda \Delta T/L$ that would occur without convection. Here, λ is the thermal conductivity of the fluid.

In Eq. 2 we already defined the slope S_{Ro} of $\mathrm{Nu}_r(1/Ro)$. Below we shall also use the slope

$$S_{\mathrm{Ek}} = [\partial \mathrm{Nu}_r / \partial (1/\mathrm{Ek})]_{\mathrm{Ra}}. \qquad (9)$$

From Eq. 7 one sees that

$$S_{\mathrm{Ek}} = 2S_{\mathrm{Ro}} \sqrt{\mathrm{Pr}/\mathrm{Ra}}. \qquad (10)$$

III. GENERAL FEATURES OF THE HEAT TRANSPORT AS A FUNCTION OF 1/Ro

Before proceeding to the new results of the present investigation, we provide an overview of the different ranges of heat-transport enhancement in rotating buoyancy-driven turbulent convection and review the extent to which the various encountered phenomena are understood.

Figure 1 shows typical data sets [47] for Nu_r as a function of 1/Ro for Pr = 4.38 at constant Ra. Figures 1 (a) and (b) show data for a relatively small Ra = 2.2×10^9 and Figs. 1 (c) and (d) display measurements for the larger Ra = 1.8×10^{10}. For (a) and (c) a linear horizontal scale was used, while (b) and (d) are displayed on logarithmic horizontal scales in order to show more clearly

the dependences at small $1/\text{Ro}$. One sees that Nu_r is not a monotonic function of $1/\text{Ro}$, and that the slope S_{Ro} (see Eq. 2) changes with $(1/\text{Ro})$. For both Ra, one can identify three ranges, separated by vertical dashed lines and marked by roman numbers in Figs. 1(b,c,d).

At small Ra and $1/\text{Ro}$, Nu_r remains nearly constant and very close to one with increasing $1/\text{Ro}$ [range I in Fig. 1 (b)]. In range II Nu_r increases as $1/\text{Ro}$ increases. From a Ginzburg-Landau-like model, we know, that the transition between range I and II at $1/\text{Ro}_c$ is sharp (see Sec. I and [36, 37]) and the increase of Nu_r beyond it is initially (locally) linear. At larger $1/\text{Ro}$ the slope decreases and Nu_r reaches a maximum $\text{Nu}_{r,max}$ at $1/\text{Ro}_{max}$. Beyond $1/\text{Ro}_{max}$ Nu_r decreases again (range III).

When with further increase of $1/\text{Ro}$ Nu_r has decreased to the point where it is less than one, it eventually enters the geostrophic regime and thereafter the pure conduction state where $\text{Nu}_r = 1/\text{Nu}(0) << 1$ and $\text{Nu} = 1$; these ranges are not under consideration in the current paper.

While the three ranges indicated in Fig. 1(b) are clearly distinguishable at any Ra, for larger Ra the structure becomes more complex and we divide the ranges into subranges. As can be seen in Fig. 1 (c and d), for larger Ra Nu_r is only (nearly) constant for very small $1/\text{Ro}$ and then decreases towards the end of range I. Thus we define two sub-ranges Ia and Ib. One sees that there is a reduction of the heat transport due to rotation in range Ib which, to our knowledge, has not yet been elucidated. This range extends up to $1/\text{Ro}_c$ where Ekman pumping starts and Nu_r begins to increase.

Remarkably, another seemingly discontinuous change of the slope S_{Ro} is seen in Fig. 1(c) at $1/\text{Ro} \approx 0.8$ (marked by an arrow). The same transition becomes more pronounced for larger Ra and could also be observed in the bulk temperature gradient in the fluid [39]. While in ranges II and III S_{Ro} changes smoothly with increasing $1/\text{Ro}$ when $\text{Ra} = 2.2 \times 10^9$ [Fig. 1(a and b)], at larger Ra different regions of essentially constant slopes are separated by further rather sharp transitions [39].

A similar non-monotonic dependence on $1/\text{Ro}$ was found as well for several other quantities, such as the time-averaged LSC temperature-amplitude δ, the LSC cessation frequency, the rotation rate of the LSC circulation plane, and the temperature gradient near the side wall of the sample [47].

The reasons for the existence of the different ranges is understood only partially and mostly qualitatively. In range I the system does not differ in a major way from the case of no rotation in the sense that there still exists a large-scale circulation, and thermal boundary layers are still located adjacent to the plates and sustain most of the temperature difference. However, a weak Coriolis force is acting upon this system. Since in this parameter range the heat transport is determined primarily by the thickness of the thermal boundary layers, one might look for an explanation of the sub-structure of Nu_r and its Ra dependence in range I by considering the influence

of the rotation on the boundary layers. This was done in Ref. [51]; but these authors focussed primarily on the influence of a weak centripetal force on the BLs (which is usually neglected in the theory of rotating convection), and their numerical calculations were for the relatively small $\text{Ra} = 4 \times 10^7$. While they found a gradual increase of Nu_r with $1/\text{Ro}$, their model has not explained the non-monotonic structure which was found experimentally at larger Ra and which leads to the two ranges Ia and Ib.

Interesting results of the flow structure were obtained also in experiments with cylinders of aspect ratio $\Gamma = 1/2$ [48]. There, range I is larger and changes of the LSC properties in this range have been observed, such as the azimuthal rotation rate of its circulation plane and the frequency at which the LSC temporarily breaks up into two rolls, one on top of the other. However, due to the differences in the LSC structure for $\Gamma = 1$ and $\Gamma = 1/2$ it is unclear to which extent there is a relationship to the phenomena discussed here for $\Gamma = 1.00$.

Another attempt to understand this range of weak rotation was presented in Ref. [56], which extended the model of Brown and Ahlers for the flow structure of RBC without rotation [24, 25, 57] to the rotating case. However, while that work provided an interesting relationship between a number of observables, including the frequency of cessations, the amplitude, and the azimuthal velocity fluctuations of the LSC, its predictions were based on model parameters derived from fits to the experimentally determined probability distribution functions of the LSC temperature-amplitudes (J.-Q. Zhong and G. Ahlers, unpublished) which already contained the basic non-monotonic dependence on $1/\text{Ro}$. Thus we conclude that even the qualitative features of this range of weak rotation in region I have not been elucidated so far.

Qualitatively, the heat-transport enhancement for $1/\text{Ro} > 1/\text{Ro}_c$ in range II is attributed to the formation of vortices close to the top and bottom plates which form due to the action of the Coriolis force on plumes that are emitted from the BLs [29]. The vortices pump hot (cold) fluid from the bottom (top) boundary layer into the bulk region and thereby enhance the heat transport - a phenomenon referred to as *Ekman pumping*. The sharp onset for this effect at $1/\text{Ro}_c$ is attributed to the influence of the sidewalls on the formation of these vortices. Experiments and numerical simulations with cylinders of different aspect ratios have shown that $1/\text{Ro}_c$ increases with decreasing aspect ratio [35–37]. When Γ and/or $1/\text{Ro}$ are too small, vortices cannot form and heat transport is not enhanced by Ekman pumping. In analogy to equilibrium critical phenomena this finite-size effect could be described well by a Ginzburg-Landau model [36, 37].

With increasing rotation rate at constant Ra, the vortices reach deeper into the fluid and a stronger Coriolis force suppresses the turbulent motion *via* the TP effect. Therefore, the heat transport decreases with increasing rotation rate in range III. With further increase of the rotation rate the enhanced Taylor-Proudman effect suppresses more vertical fluid motion and thus the
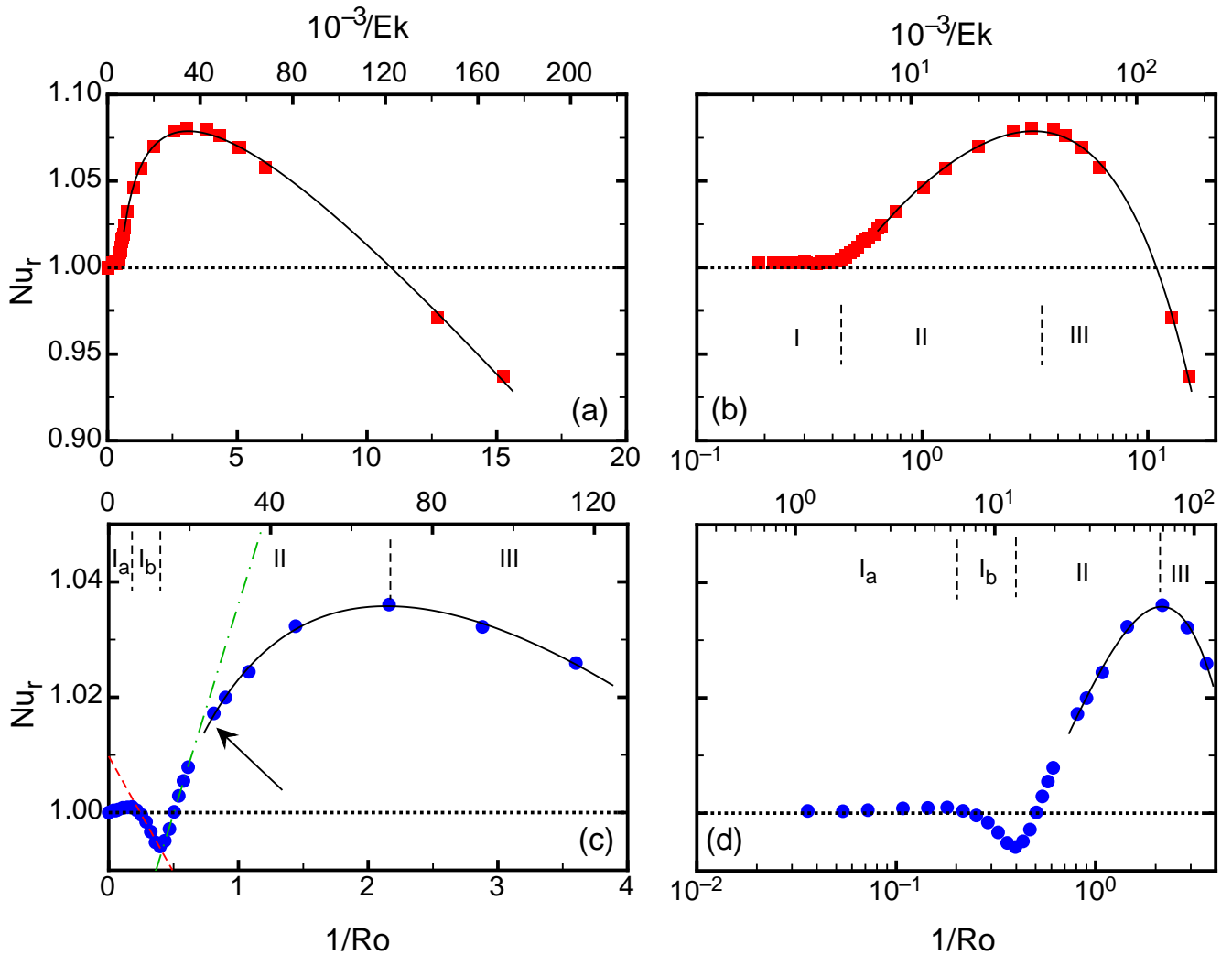
FIG. 1. (Color online). Relative Nusselt numbers Nu_r as a function of $1/Ro$ (bottom x-axis) and $1/Ek$ (top x-axis) for $Pr = 4.38$, and $Ra = 2.2 \times 10^9$ [(a) and (b)] and $Ra = 1.8 \times 10^{10}$ [(c) and (d)]. The short-dashed vertical lines in (b), (c), and (d) mark $1/Ro$ values at which the slope $\partial Nu_r/\partial(1/Ro)$ changes sign, separating different $1/Ro$-intervals. The dashed red and dash-dotted green lines in (c) show fits of linear functions based on data points close to the minimum at $1/Ro_c$. The black solid lines are fits of Eq. 15 to the data points close to the maximum $1/Ro_{max}$. The boundary between range I and II corresponds to a sharp transition at $1/Ro_c$. The arrow in (c) marks a second transition that was recently discovered and discussed in [39]. Plots (b) and (d) show the same data as (a) and (c), but on logarithmic x-axes. The uncertainties of Nu_r in these plots are indicated by the scatter of the data points and are smaller than the symbol sizes. The figure is based on data published in Ref. [47].

heat transport inside the bulk. Instead of the boundary layers, now the bulk becomes the bottleneck for the heat transport and $Nu_r < 1$.

Eventually the system enters the *geostrophic regime*, where pressure gradients are to leading order balanced by Coriolis-forces (not shown in Fig. 1). Beyond that, at the highest rotation rates, the conduction state is found with $Nu_r \ll 1$ and $Nu = 1$. The range where $Nu_r \lesssim 1$ is beyond the scope of the present paper.

IV. EXPERIMENTAL SETUP AND DATA ANALYSIS

We used cylindrical cells with aspect ratios $\Gamma \approx 1$. The experiments were done using two different apparatus; both were described in previous publications. For small-Ra measurements, we used the *small convection apparatus* (SCA). The design of this apparatus is such that it can be used with two kinds of convection cells, one that can sustain high pressures to be used with compressed gases ($Pr \lesssim 1$, see *e.g.*, Ref. [58]) and another one for liquids ($Pr > 3$, *e.g.* Ref. [59]). The apparatus was mounted on a rotating table.

Apparatus	L (cm)	fluid	Pr	Ra	Nu(1/Ro=0)
SCA	9.8	N$_2$	0.74	3.6×10^8	49.9
				9×10^8	64.7
				1.8×10^9	80.3
		SF$_6$	0.84	2.3×10^{10}	164
				4.6×10^{10}	206
	9.6	FC72	12.34	5.0×10^9	111
				9.0×10^9	131
				1.8×10^{10}	161
				2.2×10^{10}	170
MCA	24.8	water	3.05	1.2×10^9	66.6
				8×10^9	121
			3.62	4.6×10^9	102
			4.38	5.7×10^8	53.6
				2.2×10^9	81.4
				9×10^9	124
				1.8×10^{10}	153
			6.26	2.7×10^8	43.2
				2.2×10^9	80.5
			6.41	1.2×10^9	67.2
	19.0	FC72	12.34	1.9×10^{10}	164
				4.0×10^{10}	207
				1.0×10^{11}	273
				2.1×10^{11}	344
	24.1	FC72	12.34	4.2×10^{11}	421
	24.8	isopropanol	23.9	2.2×10^9	75.6
				9.0×10^9	115
			28.9	2.2×10^9	78
				9×10^9	119.3
				1.8×10^{10}	148
			35.6	2.2×10^9	78.6
				1.8×10^{10}	146.1

TABLE I. Overview of the control parameters realized in the experiments.

For small-Pr experiments the sample cell was filled with either nitrogen (N$_2$) at 34.5 bars and $T_m = 40°$C or sulfur hexafluoride (SF$_6$) at 15.2 bars and $T_m = 30°$C, resulting in Pr = 0.74 and Pr = 0.84 respectively. The sample cell was $L = 9.84$ cm high and had an inside diameter of $D = 10.16$ cm (resulting in $\Gamma = 1.03$). While the bottom plate was made of copper, the top plate was a 2.54 cm thick single-crystal sapphire disk which allowed optical access (not used in the experiments reported here). We note, that although sapphire has a significantly lower heat conductivity than copper (*i.e.*, the bottom plate), its conductivity is still more than three orders of magnitude larger than that of the working gas. Thus, assuming the top and bottom boundaries as at constant temperature is a sufficient approximation. The sidewall was made of high-tensile-strength stainless steel.

The relatively large heat conductivity of the sidewall required a relatively large correction. We corrected the
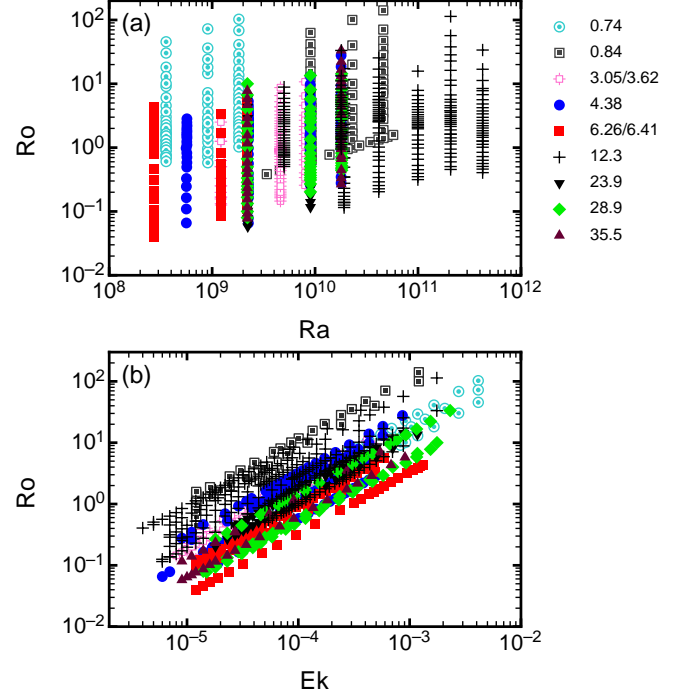

FIG. 2. (Color online). Overview of all data. The top plot shows the Ro-Ra parameter space, and the bottom plot shows the same points in the Ro-Ek parameter space. The data for Pr = 3.05, 3.62, 4.38, 6.26 and 6.41 were published already in Ref. [47] but are included in the present analysis.

measured heat transport by subtracting the heat transport measured with an evacuated cell. However, other effects of sidewall forcing (see Refs. [60, 61]) were neglected. They are of lesser importance in the case where the conductivity of the sidewall is much larger than that of the fluid, which is the case here. Further, since we are interested primarily in the relative change of the heat transport due to rotation, modest systematic errors due to the sidewall conductivity do not play an important role.

When we used the SCA with liquid, the sidewall was made of Lexan with an inner diameter $D = 9.53$ cm and a height $L = 9.96$ cm (resulting in $\Gamma = 0.96$).

We used the *Medium Convection Apparatus* (MCA) of Refs. [22, 47, 59] for measurements with liquids. Prandtl-number values of 23.9, 28.9 and 35.6 were studied using isopropanol at average temperatures $T_m = 50°$C, $40°$C and $30°$C respectively. In these experiments the height and the diameter of the convection cell were $D = L = 24.8$ cm. We also used the fluorocarbon C$_6$F$_{14}$ (3M Fluorinert$^{\mathrm{TM}}$ FC72) which yielded an intermediate Pr = 12.3 (for more information on that fluid see Ref. [22]). For these measurements T_m was $25°$C. Two samples, both with $\Gamma = 1.00$ but of different physical size, were used. The smaller one, to be designated MCA-S, had $L = D = 19.0$ cm, while the dimensions for the

larger one (MCA-L) were $L = D = 24.1$ cm. The side-walls for the MCA-S and MCA-L were made of Lexan and Acrylic, respectively. The top and bottom plates of both cells were made of copper.

Either two (SCA) or four (MCA) thermistors were placed inside the bottom plate close to its upper surface for temperature measurements. The thermistors were calibrated against a calibrated platinum thermometer in a separate apparatus before their installation in the plates. Metal-film electrical heaters were attached at the undersides of the bottom plates. The heater power was measured using a four-lead method. The copper top plate of the MCA cell had an integrated cooling system through which a cooling liquid (Ethylene glycol) circulated. The cooling-liquid temperature was set by a temperature-controlled chiller (NESLAB), such that the top plate was at the desired temperature T_t. The sapphire top plate of the SCA cell was cooled by water circulating over its top surface. The water temperature (and thus T_t) was controlled using a digital feedback loop. A small correction was applied for the temperature drop across the sapphire plate.

The rotating table and an outer structure supporting electrical and liquid feedthroughs from the laboratory to the rotating frame were similar for the SCA and the MCA, as described in detail in an earlier publication [47].

With the liquids used in the present work and various T_m the range $0.74 \lesssim \mathrm{Pr} \lesssim 35.5$ could be covered. The Rayleigh numbers ranged from 3.6×10^8 with N_2 at $\mathrm{Pr} = 0.74$ to 4×10^{11} with FC72 at $\mathrm{Pr} = 12.3$. An overview of all Pr and Ra values used is shown in Table I.

For most of the experiments, we held Ra and Pr constant, while measuring the heat transport for several different rotation rates (*i.e.* different Ro or Ek). In Fig. 2, we show all runs in the Ro-Ra and the Ro-Ek parameter space. Nu data for water ($\mathrm{Pr} = 3.05$, 4.38 and 6.26) were published before in Ref. [47] and are included in the figure and in our analysis.

V. RESULTS

A. Nusselt-number measurements

In this section we present new measurements of $\mathrm{Nu}(\mathrm{Ra}, \mathrm{Pr}, 1/\mathrm{Ro})$ before proceeding, in Sec. V B, to a global analysis of all available data.

1. Nu_r for FC72 and Isopropanol – large Pr

Figures 3 and 4 display results for Nu_r as a function of $1/\mathrm{Ro}$ for large Pr. The data were taken with FC72 (Fig. 3, Pr=12.3) and isopropanol (Fig. 4, Pr = $23.9, 28.9$, and 35.6). The results for $\mathrm{Pr} = 12.3$ are qualitatively consistent with those for water ($\mathrm{Pr} = 4.38$) shown in Fig. 1 (compare also with results for other Ra

and nearby Pr [47]) in that they reveal the three heat-transport regimes. However, they extend to larger Ra by more than a decade. The different Nu_r behaviour in the different $1/\mathrm{Ro}$ ranges is clear. After a range I_a where Nu_r does not change much, Nu_r decreases (I_b) and reaches a minimum at $1/\mathrm{Ro}_c$. As seen for the water data at smaller Pr, the transition from range I to range II at $1/\mathrm{Ro}_c$ is, within the resolution of the data, independent of Ra. For $1/\mathrm{Ro} > 1/\mathrm{Ro}_c$ Nu_r increases again in range II. While the range of $1/\mathrm{Ro}$ covered by the data was not sufficient to reach a maximum of Nu_r for Ra=4.16×10^{10}, data at both smaller and larger Ra did show such a maximum $\mathrm{Nu}_{r,max}$ at $1/\mathrm{Ro}_{max}$ after which, in range III, Nu_r decreased again. One sees that the largest value of both $\mathrm{Nu}_{r,max}$ and $1/\mathrm{Ro}_{max}$ is reached for the smallest Ra. These trends are qualitatively consistent with data obtained using water.

Especially the Nu_r-data for the two largest Ra show further rather sharp transitions above $1/\mathrm{Ro}_c$. While the detailed nature of the states above and below these transitions still needs to be elucidated, this phenomenon was discussed at length in a previous publication [39].

The trend of a diminishing $Nu_{r,max}$ with increasing Ra of the data for $\mathrm{Pr} = 12.3$ that is shown in Fig. 3 is consistent with previous results for $\mathrm{Pr} = 5.9$, Ra = 4.3×10^{15} [62] which revealed a slow decrease of Nu_r with increasing $1/\mathrm{Ro}$, without any evidence of a maximum.

Experimental results for isopropanol (Pr=23.9, 28.9, and 35.5), are shown in Fig. 4. There is a larger heat-transport enhancement for these larger values of Pr than was seen at smaller Pr. None of the data extend to $1/\mathrm{Ro}_{max}$ where Nu_r reaches $\mathrm{Nu}_{r,max}$. Nevertheless, for the smallest Ra heat-transport enhancement of up to 40% was reached, and thus $\mathrm{Nu}_{r,max}$ is even larger than 1.4.

In general, these data are qualitatively similar to the water data in Ref. [47]. For larger Ra there is a $1/\mathrm{Ro}$ range where Nu_r decreases until it reaches a minimum (range I), followed by a $1/\mathrm{Ro}$-range where Nu_r increases (range II). Again, we could not observe the maximal Nu_r and the change to range III, but we see that the slope S_{Ro} (Eq. 2) decreases with increasing $1/\mathrm{Ro}$. The rather abrupt changes of S_{Ro} observed for $\mathrm{Pr} = 12.3$ cannot be seen here. Apparently these sharp transitions become more noticeable at the larger Ra values.

2. Nu_r for N_2 and SF_6 – Pr near one

We show in Fig. 5 the data for Nu_r as a function of $1/\mathrm{Ro}$ for Pr=0.74 and Pr=0.84. One sees that the heat-transport enhancement is quite small or absent. For the smallest Ra (Ra $= 3.6 \times 10^8$) the increase of Nu_r at its maximum is only 2%. A very small enhancement was observed also in numerical simulations for Ra $= 2 \times 10^8$, albeit for a cylindrical sample with $\Gamma = 0.5$ [63]. Simulations for $\Gamma = 1$, $\mathrm{Pr} = 0.7$, and Ra $= 10^8$ [52] are shown in Fig. 5 as black triangles. They agree with our experimental data fairly well. Even a slight enhancement of
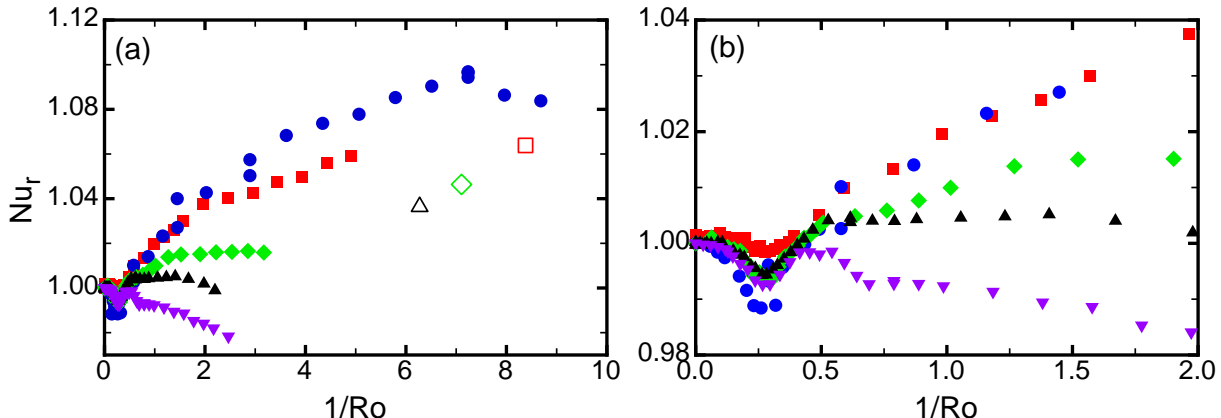
FIG. 3. (Color online). Relative Nusselt numbers Nu_r for measurements at Pr=12.34 (FC72) and Ra $= 1.91 \times 10^{10}$ (bullets, blue online), 4.16×10^{10} (squares, red online), 1.00×10^{11} (diamonds, green online), 2.07×10^{11} (up-pointing triangles, black online), and 4.24×10^{11} (down-pointing triangles, purple online). The right plot shows the same data as the left one, but zoomed closer to the onset of heat-transport enhancement. The uncertainty of the data is represented by their scatter and decreases with increasing ΔT (i.e., increasing Ra). For the three largest Ra, the uncertainty is smaller than the symbol size. Open symbols mark predictions of the maximum heat transport, as explained in Sec. V B 4. Data for Ra $= 2.07 \times 10^{11}$ and 1.00×10^{11} were published already in Ref. [39].

about 1.5% is visible. However, since the enhancement is represented by only one point, the authors of Ref. [52] apparently considered it an outlier since they stated "...no heat transport enhancement is found for Pr $= 0.7...$". Similar to experiments at larger Pr, the heat-transport enhancement is larger for smaller Ra. For Ra $\geq 1.8 \times 10^9$, no enhancement can be found.

The exact reason for the strongly reduced heat-transport enhancement at lower Pr is not known. It was argued that the larger heat diffusion makes Ekman pumping less efficient for smaller Pr [46, 52]. Warm fluid that is transported by Ekman pumping across the bottom boundary looses its heat in the horizontal direction more quickly. While this may enhance the vertical temperature gradient in the bulk, it reduces the gradient in or near the boundary layers. We also note, that small Pr indicates small Ekman-layer thicknesses δ_E.

We also show in fig. 5 the location of the expected $1/\text{Ro}_c$ (dashed vertical line), as estimated from the power-law relation between Pr and $1/\text{Ro}_c$ (see Sec. V B). No significant change is observed at this position. Noteworthy is the fact that the initial increase and the maximum of Nu_r seen for small Ra occurs before the estimated $1/\text{Ro}_c$. This implies that the enhancement of less than 2% is not caused by Ekman pumping, but rather by another still unknown mechanism. We note that the absence of any signature in Nu_r at the expected location of $1/\text{Ro}_c$ does not imply the absence of a transition. Presumably even for small Pr, where Ekman pumping is too feeble to be noticeable in the heat transport [46, 52], the formation of Ekman vortices from plumes still takes place when a critical value of $1/\text{Ro}$ has been exceeded. In this parameter range one then would have to identify the

transition on the basis of the $1/\text{Ro}$ dependence of other properties, such as internal temperature gradients [39] or other local measurements.

B. Dependence of Nu_r on Pr and Ra

1. Qualitative trends

In this section we examine all available data in order to learn about the Pr and Ra dependence of Nu_r. To this end we show in Fig. 6 three plots, each for a given Ra, of Nu_r as a function of $1/\text{Ro}$ for different Pr. The plots are for Ra $= 2 \times 10^9$ (top row), 9×10^9 (middle), and 18×10^9 (bottom). The left column shows the whole available $1/\text{Ro}$-range on a logarithmic x-axis. The right column shows only the range $1/\text{Ro} \leq 2$ on a linear scale in order to focus more closely on $1/\text{Ro}_c$ where the heat-transport enhancement sets in.

The maximal enhancement $Nu_{r,max}$ of Nu_r is seen most clearly by eye in the left column. As already apparent from Fig. 4, the largest enhancement occurs for the two largest Pr of 35.5 (brown up-triangles) and 28.9 (black down-triangles). For these Pr values the rotation rates $1/\text{Ro}_{max}$ at which the heat transport reaches its maximum could not be reached in the experiment, but the available data already show an increase of Nu_r by up to 40%. In Fig. 6a, there are only two maxima visible (for Pr $= 6.26$ and 4.38). It becomes apparent that $Nu_{r,max}$, as well as its location $1/\text{Ro}_{max}$, increase with Pr. The same trend is also shown for larger Ra in Fig. 6(c) and (e), although there $Nu_{r,max}$ is smaller. These results are in general agreement with numerical simulations [52]. Also
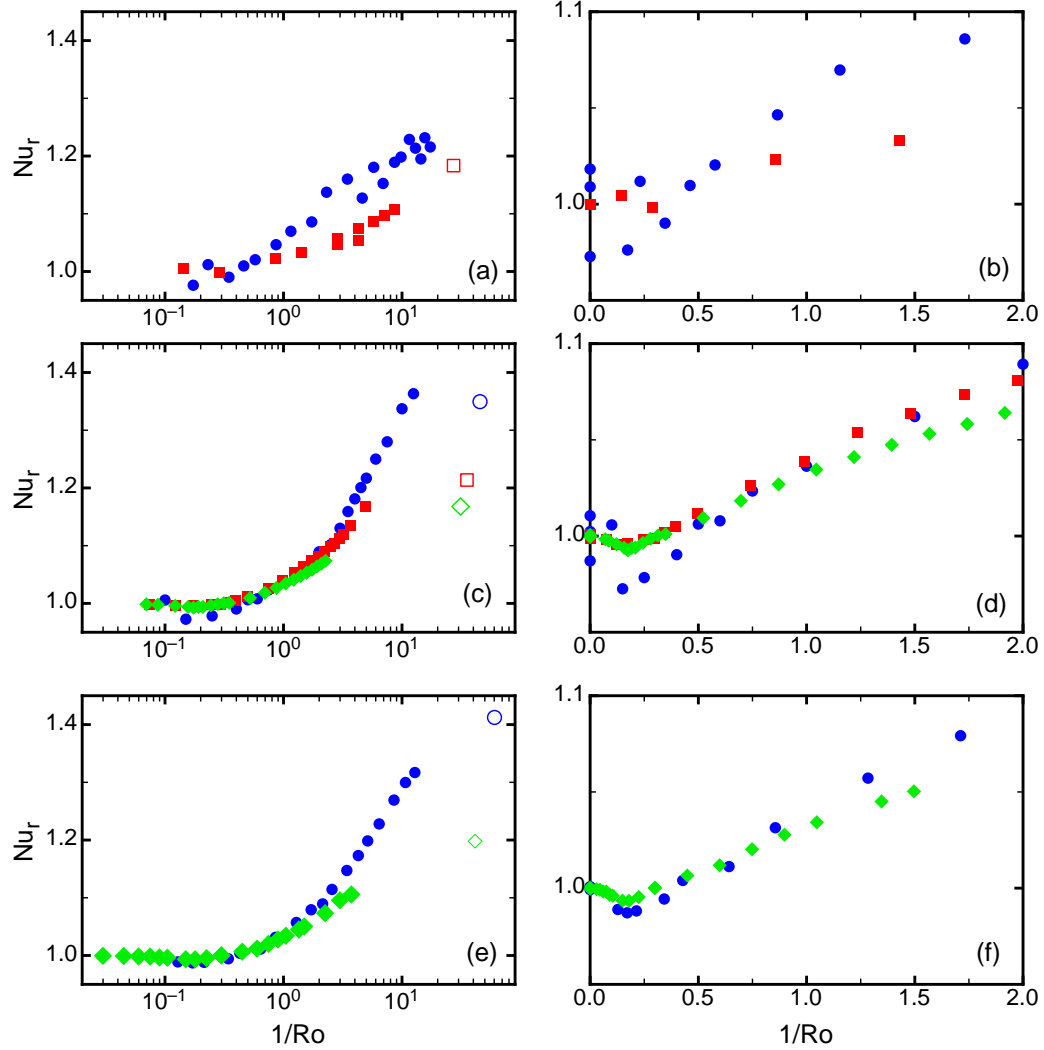
FIG. 4. (Color online). The reduced Nusselt number Nu_r for isopropanol and $Pr = 23.9$ (a and b), 28.9 (c and d) and 35.5 (e and f). The different symbols stand for $Ra = 2.2 \times 10^9$ (bullets, blue online), 9.0×10^9 (squares, red online) and 1.8×10^{10} (diamonds, green online). The left column [(a), (c), and (e)] covers a wide range of $1/Ro$ on a logarithmic scale, while the right column [(b), (d), and (f)] gives more detail at smaller $1/Ro$ on a linear scale. The uncertainty of the data is represented by the scatter of the data points. Open symbols in (a), (c), and (e) mark predictions of $Nu_{r,max}$ as explained in Sec. V B 4.

in agreement is the fact that, for the very low $Pr \simeq 1$, there is no or only a very small Nu-enhancement as discussed above in Sec. V A 2.

Looking closer at Fig. 6a, one also sees that there is a range $0.4 < 1/Ro < 3$ over which the slope S_{Ro} of $Nu_r(1/Ro)$ is independent of or at most weakly dependent on Pr. Over that range all data points within their scatter collapse onto a single curve. For larger $1/Ro$ the data diverge from each other. For $Pr \leq 6.26$ they reach their maxima and decrease afterwards, while for larger Pr they continue to increase over our $1/Ro$ range. The seemingly equal slope just above the onset of heat-transport enhancement can also be seen for larger Ra in Fig. 6(c) and (e). However, we shall show below that the initial slope does depend, albeit only weakly, on both Ra and Pr

when analyzed in more detail and over a wider parameter range.

In this context it is also noteworthy that, for the smallest Ra ($Ra = 2 \times 10^9$) in Fig. 6 and near our largest $1/Ro$, Nu_r near our largest Pr decreases with increasing Pr (see brown and black triangles in Fig. 6a). A similar behavior was found in numerical simulations [52] (see for instance Fig. 2 of that reference where Nu_r decreases with increasing Pr for $1/Ro = 10$ and $Pr \gtrsim 15$). There, they found for various constant $1/Ro$ and Ra, optimal Pr for which Nu_r was maximal. A direct comparison with the numerical results is not possible, however, because the DNS was done at smaller Ra ($Ra = 10^8$) than the experiment.

In the following sections we analyze the data sets more quantitatively and investigate how the (i) onset of heat-
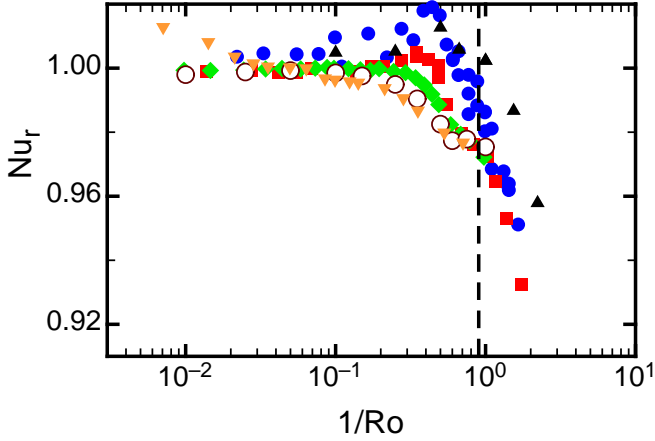
FIG. 5. (Color online). Reduced Nusselt number for compressed gases. Data show Nu_r as a function of $1/Ro$ for $Ra = 3.6 \times 10^8$ (bullets, blue online), $Ra = 9 \times 10^8$ (squares, red online), $Ra = 1.8 \times 10^9$ (diamond, green online), $Ra = 2.3 \times 10^{10}$ (open circles, brown online) and $Ra = 4.6 \times 10^{10}$ (down triangle, orange online). Data for the three lowest Ra were acquired using nitrogen ($Pr = 0.76$), the two datasets for the larger Ra were acquired using SF_6 ($Pr = 0.84$). We also show data from numerical simulations at $Ra = 10^8$ (up-triangles, black online) from Ref. [46]. The uncertainty of the data is represented by the scatter of the data points. The dashed vertical line marks the predicted onset of heat-transport enhancement based on the fit shown below in Fig. 7.

transport enhancement at $1/Ro_c$, (ii) the initial slope S_{Ro}, and (iii) the maximal heat-transport enhancement $Nu_{r,max}$ change with Ra and Pr.

2. The onset of heat-transport enhancement

Heat-transport enhancement due to Ekman pumping sets in at a particular $1/Ro_c$, causing a sharp transition with a discontinuous slope S_{Ro}. There is a small decrease of Nu_r right before $1/Ro_c$ (range Ib), leading to an effective reduction of the heat transport and a local minimum $Nu_{r,min}$ at $1/Ro_c$.

In previous papers [36, 37] it was argued that a sharp onset at a finite $1/Ro_c$ is due to the finite lateral dimension of the cylinder. Experimental measurements of $1/Ro_c$ for several aspect ratios $\Gamma = D/L$ indicated that $1/Ro_c \to 0$ as $\Gamma \to \infty$ (*i.e.* as the diameter $D \to \infty$). A Ginzburg-Landau-like equation [64] for the vortex density in a plane in the bulk but close to the thermal boundary layers, with appropriate boundary conditions, modeled the phenomenon as a finite-size effect. Consistent with this interpretation of the experimental results, simulations for the same parameters as the experimental measurements [36] found that the vortex density increases with $1/Ro$ when $1/Ro \geq 1/Ro_c$. Recent vortex-visualization experiments also showed that the vortex density has a maximum close to the side wall (although

it vanishes at the wall) when $1/Ro$ is not too large, suggesting that vortices tend to repel each other [50].

In order to illustrate the transition at $1/Ro_c$, we plot in Fig. 6(b, d and f) Nu_r over a limited range of $1/Ro$ on linear scales. The data for $Ra = 2 \times 10^9$ scatter significantly for small $1/Ro$ and thus a precise value of $1/Ro_c$ cannot be obtained. However, for $Ra = 2 \times 10^{10}$ (Fig. 6f) the onset at $1/Ro_c$ is clearly visible. Here we see that $1/Ro_c$ depends on Pr, being smaller for larger Pr.

To quantify the location of $1/Ro_c$, we fit the function

$$Nu_r = \begin{cases} S^-_{Ro}/Ro + n & ; 1/Ro < 1/Ro_c \\ S^+_{Ro}/Ro + (S^-_{Ro} - S^+_{Ro})/Ro_c + n & ; 1/Ro > 1/Ro_c \end{cases} \tag{11}$$

to the data points close to the onset. In this way we get not only $1/Ro_c$, but also the slopes S^-_{Ro} and S^+_{Ro} just below and above $1/Ro_c$ and the minimal relative Nusselt number $Nu_{r,min} = S^-_{Ro}/Ro_c + n$ which occurs at $1/Ro_c$ [65].

In Fig. 7a we show $1/Ro_c$ as a function of Pr on double-logarithmic scales. The data can be represented by a straight line and a fit yielded the power law

$$1/Ro_c = K_1 \cdot Pr^\alpha \tag{12}$$

with an exponent $\alpha = -0.41 \pm 0.02$ and a coefficient $K_1 = 0.75 \pm 0.02$. A very similar behaviour with nearly the same exponent (within its margin of error) was already found before [47]. There, however only data acquired with water as the convective fluid were used, spanning the rather short Pr interval of $3.05 \leq Pr \leq 6.26$. To our knowledge the mechanism that yields the Pr dependence of $1/Ro_c$ remains to be elucidated.

From Fig. 6b it appears that the influence of Ra on the location of $1/Ro_c$ is very weak or absent. In order to search for a small effect, we plot in Fig. 7b the reduced form $Pr^{0.41}/Ro_c$ as a function of Ra so as to remove the effect of Pr. We see no trend in these data. Thus, within the resolution of the data Ra has no influence on the location of $1/Ro_c$ in the range $10^9 < Ra < 10^{12}$, and the coefficient K_1 in Eq. 12 is within experimental uncertainty independent of Ra. We note that Eq. 7 then implies that the transition value of the inverse Ekman number $1/Ek_c$ is proportional to $Ra^{0.50}$ and $Pr^{\alpha-1/2} = Pr^{-0.91}$.

3. The slopes before and after $1/Ro_c$

By fitting Eq. 11 to the data for $Nu_r(1/Ro)$ near $1/Ro_c$, we also obtained the slopes S^-_{Ro}, S^+_{Ro}, and the reduced Nusselt number $Nu_{r,min}$ at the onset.

Zhong and Ahlers [47] show plots of S^+_{Ro} as a function of Ra and Pr (see fig. 7 of Ref. [47]). They found no dependence of S^+_{Ro} on Ra, but a seemingly significant increase with Pr corresponding to a power law with an exponent of 0.27. However, their data covered only a small range of Pr and an accurate determination of the
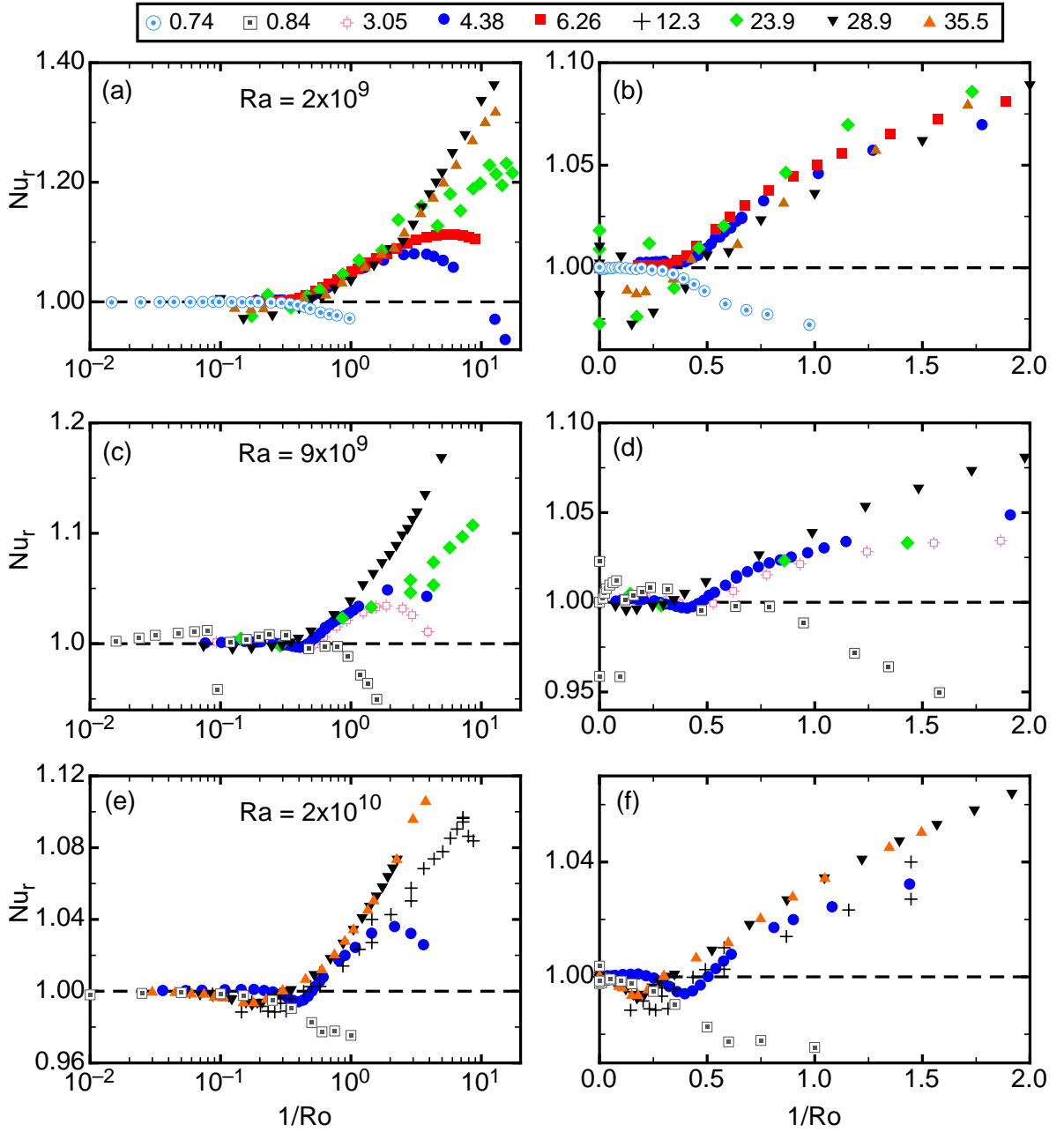
FIG. 6. (Color online). Comparison of Nu_r as a function of $1/Ro$ for different Pr and $Ra = 2 \times 10^9$ (a and b), 9×10^9(c and d), and 2×10^{10} (e and f). The left column shows the full experimentally accessible range on a logarithmically scaled x-axis. The right column shows the range $0 < 1/Ro < 2$ using a linear x-axis. Different symbols stand for different Pr as explained at the top of the figure. The horizontal black dashed line marks $Nu_r = 1$.Note that different vertical scales were used because of the different ranges of the data.

Pr dependence thus was not possible. We find that plotting the much more extensive data for S_{Ro}^+ that are now available as a function of Ra or Pr as was done in Ref. [47] does not reveal an obvious Ra-, or Pr-dependence of S_{Ro}^+. A monotonic increase of S_{Ro}^+ with Pr as suggested in Ref. [47] is not observed.

Until now, we considered the heat-transport enhancement as a function of the inverse Rossby number $1/Ro$.

This is useful since $1/Ro$ is of order unity in the range were the heat transport is enhanced, and in retrospect because it leads to a Ra-independent transition. We could have also considered the inverse Ekman number $1/Ek$ as the control parameter (top x-axis in Fig. 1). As mentioned above, the scaling of the critical inverse Ekman number at which heat-transport enhancement sets in ($1/Ek_c$) would then be different. In addition, the slope
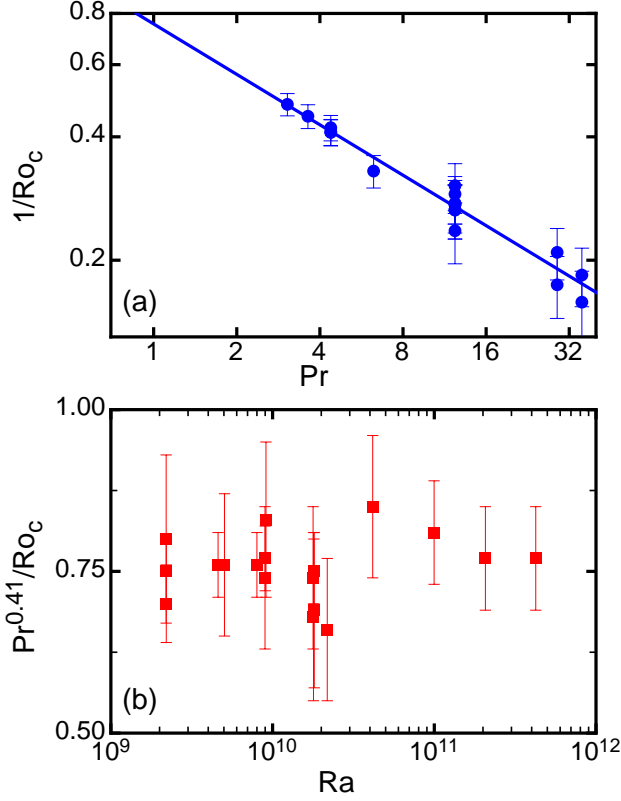
FIG. 7. (Color online). (a): Critical inverse Rossby number as a function of Pr on a double logarithmic plot. Blue solid line marks the fitted power law with an exponent $\alpha = -0.41$. (b): Reduced critical inverse Rossby number as a function of Ra. The y-axis is linearly scaled. The x-axis is on a logarithmic scale.

FIG. 8. (Color online). (a): The slope of the initial heat-transport enhancement S_{Ek}^+ as a function of Ra in a double logarithmic plot. (b): The reduced slope $S_{Ek}^+ \cdot \text{Ra}^{-0.60}$ as a function of Pr in a plot with logarithmic x-axis and linear y-axis. Data points are color coded corresponding to the other variable (color represents Pr in (a) and $\log_{10}(\text{Ra})$ in (b)). Straight lines are power-law fits to the data.

S_{Ek}^+ (see Eq. 9) of $\text{Nu}_r(1/\text{Ek})$ would also be different. From Eq. 7 one sees that $S_{\text{Ek}}^+ = 2S_{\text{Ro}}^+ \sqrt{\text{Pr}/\text{Ra}}$. S_{Ek}^+ has the advantage that it covers almost two orders of magnitude for our data sets, whereas S_{Ro}^+ changes only by a factor of two. In Fig. 8a we plot S_{Ek}^+ as a function of Ra. One sees that S_{Ek}^+ decreases monotonically with increasing Ra. In this double-logarithmic plot a power-law behavior $S_{\text{Ek}}^+ \propto \text{Ra}^\beta$ is visible with an exponent $\beta \simeq -0.60$. The data points in Fig. 8a are color coded with respect to their corresponding Pr. We see that greenish points (large Pr) lie in general above the fitted straight line while reddish points (low Pr), are below, suggesting that S_{Ek}^+ also depends on Pr. In order to investigate the Pr dependence, we plot in Fig. 8b the reduced slope $S_{\text{Ek}}^+ \cdot \text{Ra}^{0.60}$ versus Pr. This quantity increases with Pr, showing a power-law dependence with an exponent of about 0.31.

While these two exponents are not yet the best-fit values, they are good starting parameters for a two-
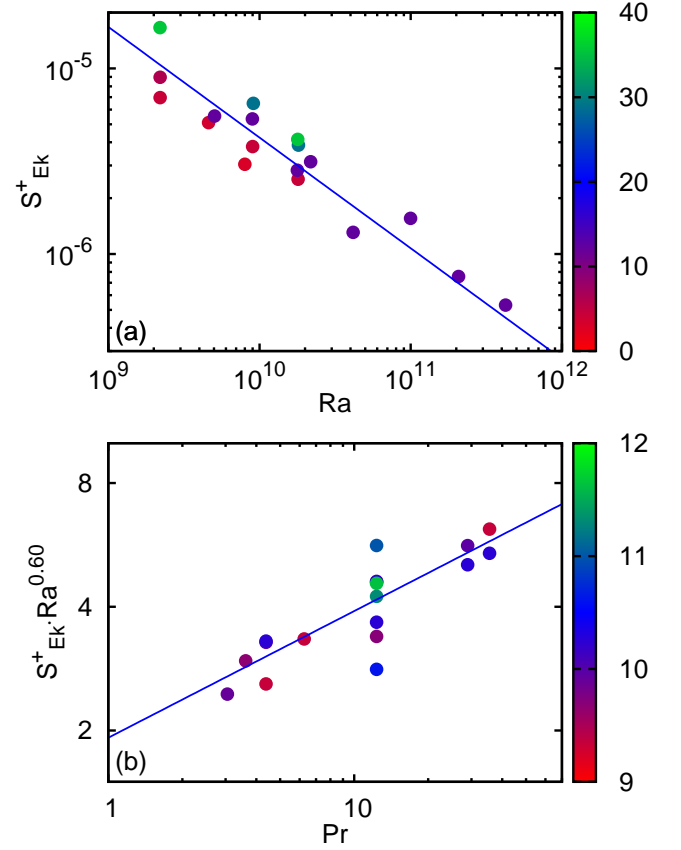
dimensional non-linear least-square fit of the equation

$$S_{\text{Ek}}^+ = K_{\text{Ek}} \text{Pr}^{\tilde{\beta}_1} \text{Ra}^{\tilde{\beta}_2} \tag{13}$$

to the data. This fit yielded $\tilde{\beta}_1 = 0.34 \pm 0.05$ and $\tilde{\beta}_2 = -0.54 \pm 0.08$. Having both exponents, we plot in Fig. 9a S_{Ek}^+ as a function of $\text{Pr}^{\tilde{\beta}_1} \cdot \text{Ra}^{\tilde{\beta}_2}$. We see that all data points lie on a straight line. A linear fit gives a slope of $K_{\text{Ek}} = 0.5 \pm 0.02$ and a negligible intercept of $n < 10^{-6}$. From this consideration we calculate that S_{Ro}^+ can similarly be expressed as

$$S_{\text{Ro}}^+ = K_{\text{Ro}} \cdot \text{Pr}^{\beta_1} \text{Ra}^{\beta_2}. \tag{14}$$

with $\beta_1 = -0.16 \pm 0.05$ and $\beta_2 = -0.04 \pm 0.08$. Figure 9b shows S_{Ro}^+ plotted as a function of $\text{Pr}^{-0.16}\text{Ra}^{-0.04}$. Again, the data points follow a straight line, in this case with a slope $K_{\text{Ro}} = 0.3 \pm 0.05$. The scatter seems larger than it is for S_{Ek}^+; however, this is merely due to the
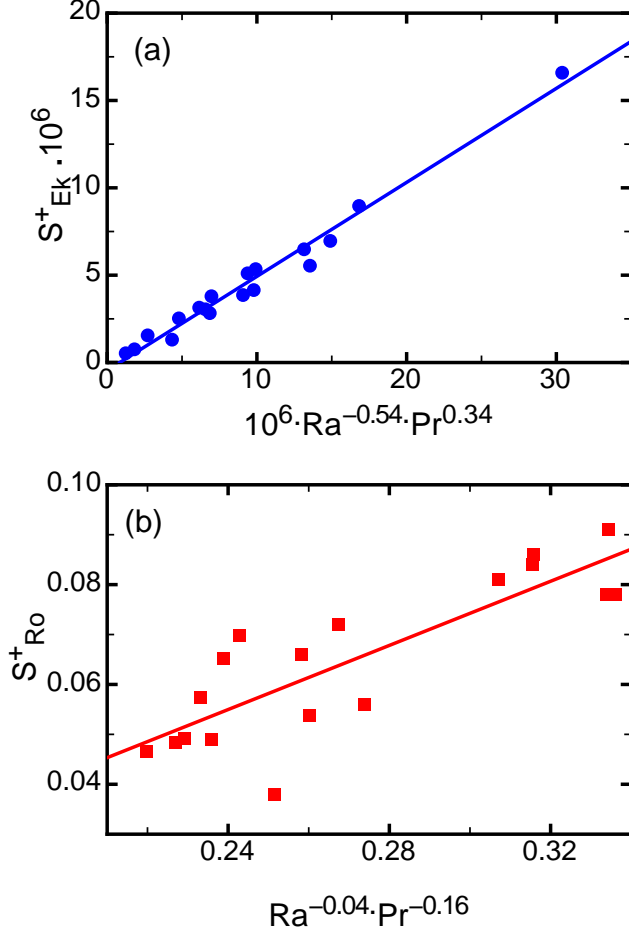
FIG. 9. (Color online). Master curves of the slope of the initial heat-transport increase S^+_{Ek} (a) and S^+_{Ro} as a function of Pr and Ra.

FIG. 10. (Color online). The slopes S^-_{Ro} before $1/\mathrm{Ro}_c$ as a function of Ra (a, color represents Pr) and Pr (b, color represents $\log_{10}(\mathrm{Ra})$).

rather small range of S^+_{Ro} which also leads to a larger uncertainty of K_{Ro}.

We note, that the results for β_1 and β_2 differ from those found by analyzing only only the water data was done in Ref. [47] and which yielded $S^+_{Ro} = 0.058\mathrm{Pr}^{0.27}$ (no dependency of Ra). This difference is because we: (i) used a significantly larger dataset, (ii) analysed the data in a truly two-dimensional way that takes Ra and Pr dependency into account, and (iii) analysed the data first in terms of $1/\mathrm{Ek}$ and later converted S^+_{Ek} to S^+_{Ro}.

The slope right before $1/\mathrm{Ro}_c$ (S^-_{Ro}) is shown in fig. 10. Even though the data scatter significantly, one can see that S^-_{Ro} decreases with increasing Ra and increasing Pr. While S^-_{Ro} is positive for the smallest Ra and Pr (red bullets), it becomes slightly negative as Ra or Pr increase. However, a quantitative analysis is difficult and in particular a separation of the Ra and Pr dependences was not possible.
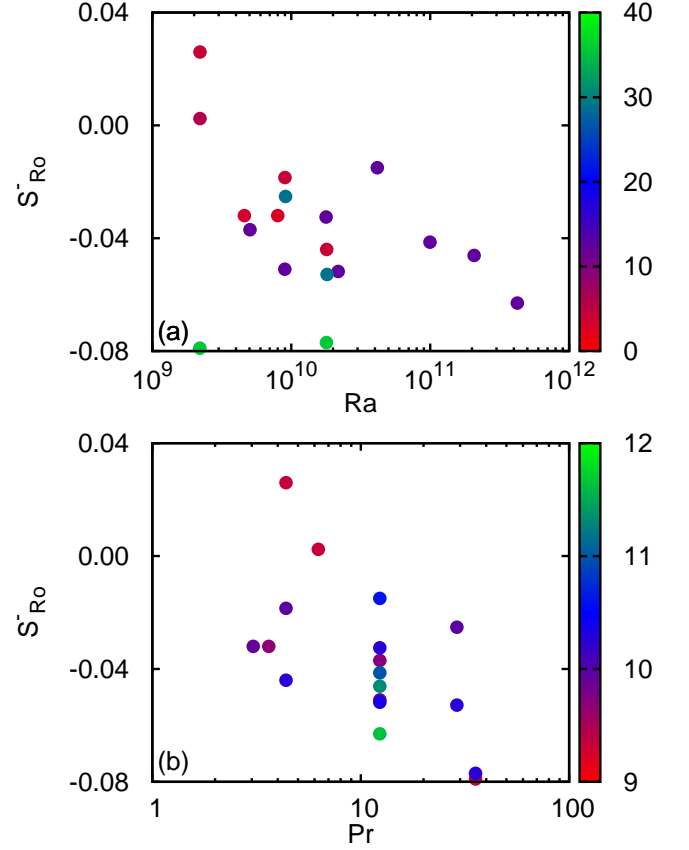
Another parameter obtained from fitting eq. 11 to the data is the Nusselt number at $1/\mathrm{Ro}_c$ ($\mathrm{Nu}_{r,min}$). In order to investigate its dependence on Ra and Pr, we plot $\mathrm{Nu}_{r,min}$ in Fig. 11 as a function of Ra (Fig. 11a) and as a function of Pr (Fig. 11b). We include qualitatively in each of the plots the dependence on the other variable using the color code shown to the right of the figures. One sees that $\mathrm{Nu}_{r,min}$ depends only very weakly on Ra and Pr. The largest and the smallest values differ by less than 2%. There is a general trend of $\mathrm{Nu}_{r\,min}$ to smaller values as either Ra or Pr increase, but it is difficult to draw strong conclusions from Fig. 11.

4. Maximum heat-transport enhancement

Above we saw that the maximal heat transport $\mathrm{Nu}_{r,max}$ and its location at $1/\mathrm{Ro}_{max}$ depend strongly on Ra and Pr (see *e.g.* Figs. 1, 3, 4, 6, and also Ref. [47]). We pointed out already in Sec. V B that (at constant Pr) $\mathrm{Nu}_{r,max}$ is smaller for larger Ra and (at constant Ra) increases with increasing Pr. With increasing $\mathrm{Nu}_{r,max}$ $1/\mathrm{Ro}_{max}$ increases as well and for large Pr it is located
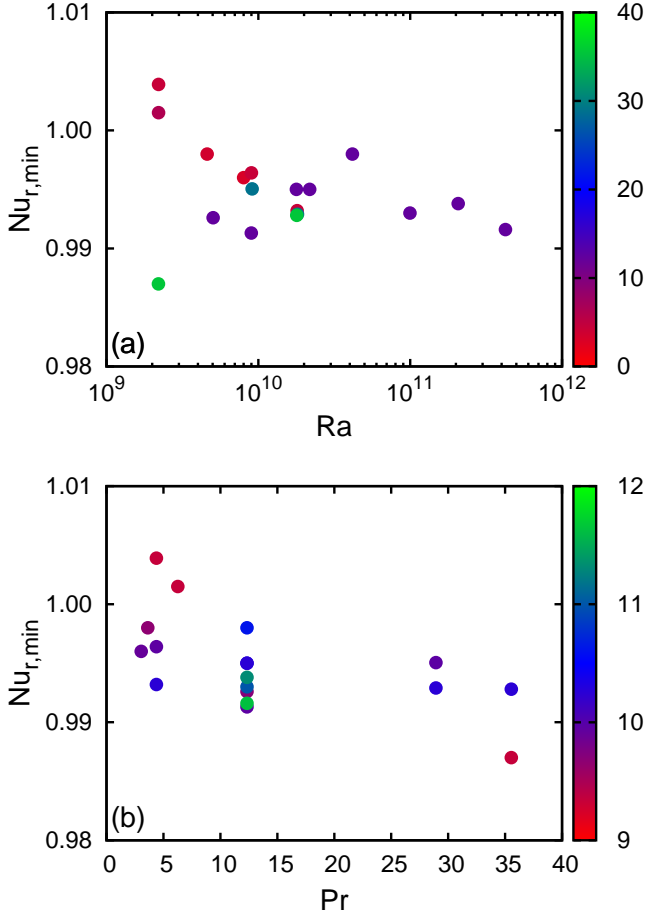
FIG. 11. (Color online). Nusselt number at $1/\mathrm{Ro}_c$ ($\mathrm{Nu}_{r,min}$) as a function of Ra (a, color represents Pr) and Pr (b, color represents $\log_{10}(\mathrm{Ra})$).

beyond the experimentally accessible $1/\mathrm{Ro}$-range. For $\mathrm{Pr} = 12.3$ (see Fig. 3), where all data are for relatively large Ra, Nu_r shows a well defined maximum only at $\mathrm{Ra} = 1.9 \times 10^{10}$. As Ra increases further, a plateau of constant or slowly varying Nu_r develops, with sharp transitions, involving large changes of the slope S_{Ro}, bordering the plateau at larger and smaller $1/\mathrm{Ro}$. Clearly this behavior does not lend itself to the smooth power-law representations explored in the present paper.

In order to estimate $\mathrm{Nu}_{r,max}$ and $1/\mathrm{Ro}_{max}$, we fit the function

$$f(x) = a \cdot \log(x - x_0) + bx + c \; ; \quad x = 1/\mathrm{Ro} \qquad (15)$$

to the data points close to $1/\mathrm{Ro}_{max}$, adjusting a, x_0, b, and c. Examples of such fits are shown in Fig. 1. Over a wide range of Ra this function represents the data remarkable well. It takes the asymmetry of the peak into consideration while assuring the existence of only a single maximum (in contrast to a 3rd order polynomial for instance). In this way, we can determine $1/\mathrm{Ro}_{max}$ and

$\mathrm{Nu}_{r,max}$ with better accuracy than by just using the data points with the larges Nu_r. We appreciate that this procedure is questionable at very large Ra where the discontinuities of S_{Ro} are dominating the shape of $\mathrm{Nu}_r(1/\mathrm{Ro})$.

Since we are mostly interested in the additional heat transported due to rotation, we focus on $\mathrm{Nu}_{r,max} - 1$. It would be convenient to find a simple power-law representation

$$\mathrm{Nu}_{r,max} - 1 = M_{\mathrm{Ro}}\mathrm{Pr}^{\delta_1}\mathrm{Ra}^{\delta_2} \qquad (16)$$

of the data. However, plotting $\mathrm{Nu}_{r,max} - 1$ as a function of either Ra or Pr for all data points does not show a significant trend in either of these plots (not shown here), and an immediate two-dimensional least-squares fit of Eq. 16 to the data was not successful without a good guess at the initial values of the parameters. Thus, we take an approach similar to that of Sec. V B 3, *i.e.* we first plot $\mathrm{Nu}_{r,max} - 1$ as a function of Pr and fit the power law $\mathrm{Nu}_{r,max} - 1 = a_1 \cdot \mathrm{Pr}^{\delta_1}$ to it. The value of δ_1 is then used to create a reduced form $(\mathrm{Nu}_{r,max} - 1) \cdot \mathrm{Pr}^{-\delta_1}$, which we plot as a function of Ra. A similar fit of $\mathrm{Nu}_{r,max} - 1 = a_2 \cdot \mathrm{Ra}^{\delta_2}$ gives the exponent δ_2 that we again use to plot the first reduced form $(\mathrm{Nu}_{r,max} - 1) \cdot \mathrm{Ra}^{-\delta_2}$ *vs.* Pr and so on. In this iterative way, the exponents converge quickly (after 4 iterations) to $\delta_1 = 0.65$, $\delta_2 = -0.35$.

Figure 12 shows the results of the last iterations. One sees that a power-law dependence on Pr and Ra agrees fairly well with the data. However, while the data cover two orders of magnitude of Ra, they span less than a single order of magnitude of Pr. In addition one sees in Fig. 12a that points for small Pr and for the largest Pr are below the fitted line, whereas points in between are above it. Because of this, δ_1 is sensitive to the data used in the fit. Removing the point at the highest Pr=23.9 increases δ_1 by 20%, while δ_2 changes by only 5% change.

The above procedure gave excellent initial values for a direct two-dimensional fit of Eq. 16 to the data. That fit yielded $\tilde{M}_{\mathrm{Ro}} = 42 \pm 27$, $\tilde{\delta}_1 = 0.80 \pm 0.08$ and $\tilde{\delta}_2 = -0.35 \pm 0.03$. Again, while the Pr exponent differs, the Ra exponent stays unchanged. The reason for the different results from the two methods is that data points in the two approaches are weighted differently. In the least-squares-fit method, every data point has equal weight. The single point at $\mathrm{Pr} = 23.9$ has little influence since there is a large cluster of points between $\mathrm{Pr} = 3$ and 6.3. In the iterative approach the point at $\mathrm{Pr} = 23.9$ gets more weight and thus the exponent decreases significantly.

We show in Fig. 13 plots of Nu_{rmax} as a function of both, $\mathrm{Pr}^{\delta_1} \cdot \mathrm{Ra}^{\delta_2}$ (blue bullets) and $\mathrm{Pr}^{\tilde{\delta}_1} \cdot \mathrm{Ra}^{\tilde{\delta}_2}$ (red squares). As expected, the points follow their corresponding linear master curves. The slopes are found to be $M_{\mathrm{Ro}} = 64 \pm 2$ and $\tilde{M}_{\mathrm{Ro}} = 44 \pm 2$, respectively.

The situation for $1/\mathrm{Ro}_{max}$ is similar. We applied a similar iterative method as above to reveal a potential power-law relationship of the form

$$1/\mathrm{Ro}_{max} = N_{\mathrm{Ro}}\mathrm{Pr}^{\epsilon_1}\mathrm{Ra}^{\epsilon_2} \; . \qquad (17)$$
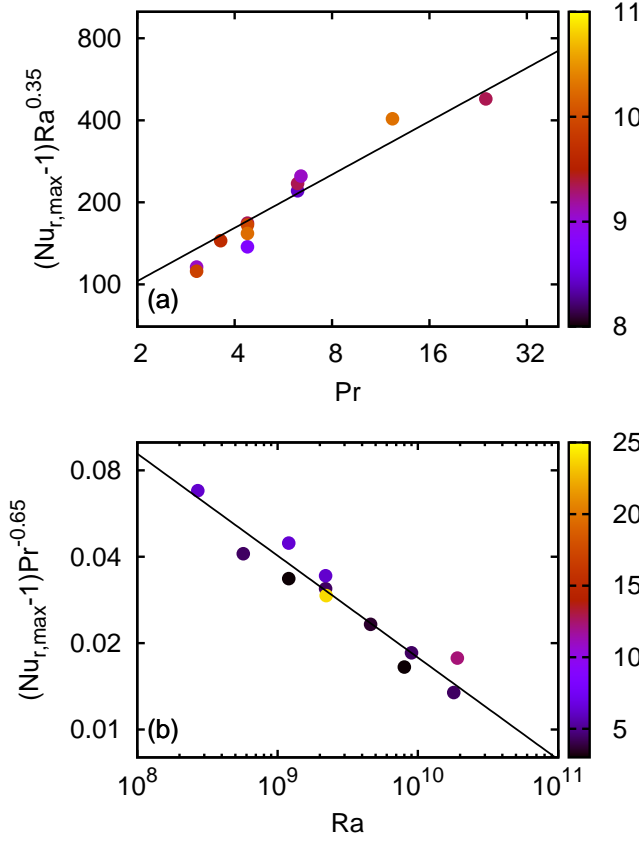
FIG. 12. (Color online). (a): Rescaled heat-transport enhancement $(\mathrm{Nu}_{r,max} - 1) \cdot \mathrm{Ra}^{0.35}$ as a function of Pr. Color of the symbols stands for the $log_{10}(\mathrm{Ra})$. (b): Rescaled heat-transport enhancement $(\mathrm{Nu}_{r,max} - 1) \cdot \mathrm{Pr}^{0.65}$ as a function of Ra. Color of each symbol represents Pr.
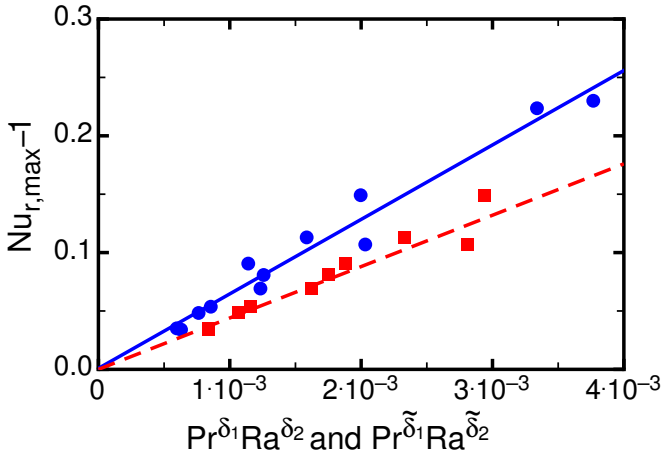

FIG. 13. (Color online). The maximal heat-transport enhancement $\mathrm{Nu}_{r,max} - 1$ as a function of $\mathrm{Pr}^{\delta_1} \cdot \mathrm{Ra}^{\delta_2}$ (blue bullets) and $\mathrm{Pr}^{\tilde{\delta}_1} \mathrm{Ra}^{\tilde{\delta}_2}$ (red squares). The blue solid line and the red dashed line are linear fits to the data points with slopes $M_{\mathrm{Ro}} = 64$ and $\tilde{M}_{\mathrm{Ro}} = 44$.

with $\epsilon_1 = 1.45 \pm 0.06$ and $\epsilon_2 = -0.17 \pm 0.03$. This result is shown in Fig. 14 where the corresponding reduced forms of $1/\mathrm{Ro}_{max}$ are plotted as a function of Pr and Ra. One sees in Fig. 14a, that $\mathrm{Ra}^{\epsilon_2}/\mathrm{Ro}_{max}$ follows nicely a power-law dependence on Pr. The reduced $\mathrm{Pr}^{-\epsilon_1}/\mathrm{Ro}_{max}$ as a function of Ra is plotted in Fig. 14b. There the data also seem to follow a power law, although the data scatter significantly more and deviate more from the best fit. Especially the data point with the largest Ra (1.9×10^{10}), lies significantly below the fitted line. While this might be evidence that the Ra-dependence is more complicated than just a simple power law, the error of this data point is also rather large; *i.e.* there is a large uncertainty of $1/\mathrm{Ro}_{max}$.

A direct two-dimensional fit, using the exponents ϵ_1 and ϵ_2 as starting values, gives very similar exponents $\tilde{\epsilon}_1 = 1.37 \pm 0.05$ and $\tilde{\epsilon}_2 = -0.18 \pm 0.03$.
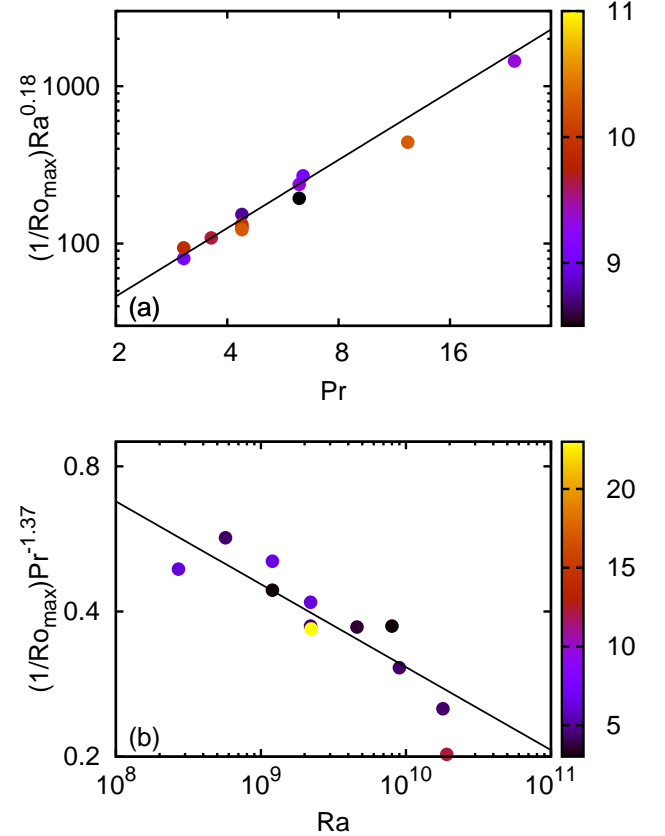

FIG. 14. (Color online). (a): Rayleigh-reduced inverse Rossby number $\mathrm{Ra}^{0.17}/\mathrm{Ro}_{max}$ at the maximum of Nu_r as a function of Pr. The decimal logarithm of the corresponding Ra is color coded. (b): Prandtl-reduced $\mathrm{Pr}^{-1.45}/\mathrm{Ro}_{max}$ as a function of Ra. The corresponding Pr is color coded. In both plots, the axes are logarithmically scaled.

In Fig. 15 we plot a master curve of $1/\mathrm{Ro}_{max}$ as a function of $\mathrm{Pr}^{1.37} \cdot \mathrm{Ra}^{-0.18}$. All data points follow a straight line with a slope $N_{\mathrm{Ro}} = 21.4 \pm 0.5$. One sees that the assumption of a power-law dependence is a good approxi-

mation. Even the single point at the right top corner still agrees with the fitted curve. We note, however, that that particular $1/Ro_{max}$ value is uncertain because it was obtained by an extrapolation of eq. 15 beyond the data used in the fit; the maximum lies beyond the experimentally accessible $1/Ro$ range as seen in Fig. 4a.
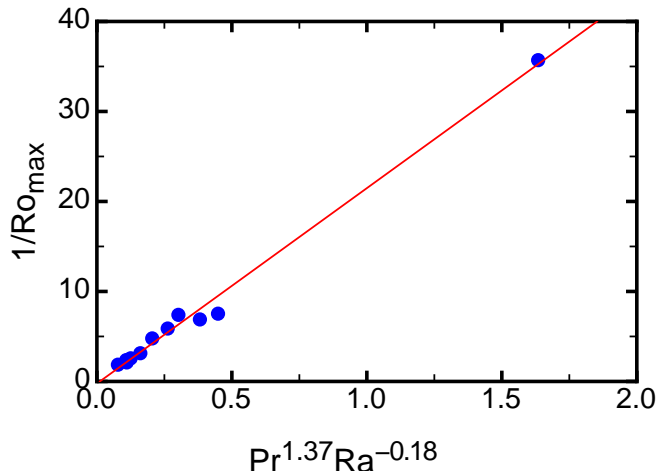

FIG. 15. (Color online). Location of the maximal heat-transport enhancement $1/Ro_{max}$ as a function of $Pr^{1.37} \cdot Ra^{-0.179}$. The data follow a linear trend (red solid line) with slope $N_{Ro} = 21.4 \pm 0.5$.

Using the calculated exponents $\delta_1 = 0.65$, $\delta_2 = -0.35$, $\tilde{\epsilon}_1 = 1.37$, and $\tilde{\epsilon}_2 = -0.18$ and the amplitudes $M_{Ro} = 64$ and $N_{Ro} = 21.4$, we can make predictions of $Nu_{r,max}$ and $1/Ro_{max}$ for the data sets for which we could not reach $1/Ro_{max}$ in the experiment. These predictions are plotted in Figs. 3 and 4 as open symbols. Let us consider first the large-Pr case (Fig. 4). In almost all cases the predicted $Nu_{r,max}$ is reasonable, with the only exception for $Pr = 28.9$ and $Ra = 2.2 \times 10^9$ where the predicted value is actually smaller than the largest measured value. For the smaller $Pr = 12.34$ we see that the prediction is convincing only for $Ra = 4.16 \times 10^{10}$. It is clearly in error for $Ra \gtrsim 10^{11}$. It is noteworthy that this is the range where sharp transitions between states, involving large changes of the slope S_{Ro}, are found; these features clearly are not captured by Eq. 15.

VI. SUMMARY AND DISCUSSION

A. New experimental data

In this paper we report on the heat-transport enhancement due to rotation in buoyancy-dominated turbulent thermal convection as a function of the Rayleigh number and the Prandtl number for samples with aspect ratio $\Gamma = 1.00$. We added experimental data for small Pr by making measurements with compressed gasses (N_2 with $Pr = 0.74$ and SF_6 with $Pr = 0.84$), for medium

Pr but exceptionally large Ra by using the fluorocarbon FC72 ($Pr = 12.3$), and for large Pr by using isopropanol ($Pr = 23.9$, 28.9, and 35.5). Together with previous data acquired with water [47] ($3.0 \lesssim Pr \lesssim 6.4$), all available measurements cover the Rayleigh-number range $4 \times 10^8 < Ra < 4 \times 10^{11}$ and values of Pr from 0.74 to 35.5. This large data set makes it possible for the first time to study quantitatively the influence of Pr on the heat-transport enhancement in rotating turbulent Rayleigh-Bénard convection.

B. Three different ranges of $1/Ro$

It was shown already [37, 39, 47, 58] that at least three different ranges of the rotation rate $1/Ro$ can be observed, with qualitative different slopes S_{Ro} (see Eq. 2) in each of them. These different ranges are illustrated in Fig. 1. Starting at small $1/Ro$, the first (I) is one of nearly constant heat transport Nu_r. For large enough Ra it can be separated into two subranges. In the first (I_a) Nu_r increase very slightly, by a few tenths of a percent. It is followed by subrange I_b where Nu_r decreases by a percent or so. In range I_a and I_b the turbulent flow is self-organized into a large-scale circulation consisting of a single convection roll (LSC). The stochastic dynamics, amplitude, and stability of the LSC are influenced by Coriolis forces as indicated by previous measurements [47, 48]. Although one might have thought that the elucidation of phenomena at these smallest rotation rates should be most accessible to theory, the origin of the two subranges I_a and I_b, and the dependence of Nu_r upon Ra in these ranges, remain unexplained at present.

Range I is followed by a range II where the heat transport increases up to a rather broad maximum. Ranges I and II are separated by a sharp transition at $1/Ro_c$. The transition marks the onset of Ekman-vortex formation due to the action of the Coriolis force on thermal plumes emitted from the boundary layers. Remarkably, in samples of finite lateral extent the vortex formation can only start after a critical value $1/Ro_c$ is exceeded. This has been explained theoretically as a finite-size effect that can be described by a Ginzburg-Landau model [36, 37]. The increase of Nu_r above $1/Ro_c$ in range II is understood to be due to the vortices near the thermal boundary layers adjacent to the top and bottom plate; these vortices cause an increased fluid transport by means of Ekman pumping from the plates across the boundary layers into the bulk. In this range the LSC is no longer stable. Its geometry is incompatible with the vortex formation, and it soon ceases to exist for $1/Ro > 1/Ro_c$.

Range II is followed by range III of decreasing heat transport. Also ranges II and III divide into subranges for larger Ra, where S_{Ro} has noticeable discontinuities at several values of $1/Ro$. The specific reasons for this subdivision need further elucidation, but are expected to be found in transitions between turbulent states with large-scale structures of different symmetries [39].

A gradual decrease with increasing $1/\mathrm{Ro}$ in range II of the slope S_{Ro}, and eventually an actual heat-transport reduction ($S_{\mathrm{Ro}} < 1$) in range III, are due to a reduced vertical fluid transport with increasing $1/\mathrm{Ro}$, caused by the Taylor-Proudman (TP) effect. While this qualitative picture is clear, a quantitative understanding of the heat-transport enhancement due to Ekman pumping and its depression due to the TP effect is still lacking.

C. Results of the present data analysis

In the present paper we carried out a correlation of new as well as previously published data describing the transitions between range I and II and between II and III. Within the resolution of the data we found that the transition between I and II at $1/\mathrm{Ro}_c$ is independent of Ra and decreases with Pr (see Fig. 7). The decrease can be described by a power law with an exponent $\alpha = -0.41$ (Eq. 12). It is very surprising that $1/\mathrm{Ro}_c$ is independent of Ra over three decades. That means, that the onset of the formation of vortices close to the boundaries does not depend on the thermal driving. However we note that an alternative choice for the dimensionless rotation rate, like the inverse Ekman or the Taylor number for example, would cause a Ra dependence of the corresponding critical values $1/\mathrm{Ek}_c$ (see Eq. 7) and Ta_c. To our knowledge there is as yet no theoretical explanation of the Pr dependence and the Ra independence of $1/\mathrm{Ro}_c$.

We determined the initial slope S_{Ro}^+ just above $1/\mathrm{Ro}_c$ by fitting a linear function with a discontinuous derivative (Eq. 11) to data points in ranges I and II but close to $1/\mathrm{Ro}_c$. The initial slope S_{Ro}^+ just above $1/\mathrm{Ro}_c$ was essentially independent of Ra and depended only weakly upon Pr (see Fig. 9). This weak dependence, and the limited data range especially for Pr, made it difficult to determine power-law exponents from a straight forward least-squares fit. It was easier to determine the Ra and Pr dependence of the slope S_{Ek}^+ derived from the dependence of Nu_r on the Ekman number Ek (Eq. 9). The results of this analysis could be transformed back to yield the power-law dependence $S_{\mathrm{Ro}}^+ \propto \mathrm{Pr}^{\beta_1}\mathrm{Ra}^{\beta_2}$ with $\beta_1 \simeq -0.16$ and $\beta_2 \simeq -0.04$. While at present these exponents remain unexplained, we expect that they may be central to a theoretical elucidation of Ekman pumping in this system.

We also investigated the location $1/\mathrm{Ro}_{max}$ and the height $\mathrm{Nu}_{r,max}$ of the maximum heat-transport enhancement. Analyzing these quantities was more difficult, since the maximum of Nu_r is broad and for large Pr was beyond the experimentally accessible range of $1/\mathrm{Ro}$. Therefore, the investigated Pr range is small and parameter uncertainties are relatively large (especially for $1/\mathrm{Ro}_{max}$). Also here we analyzed potential power-law dependences of both quantities on Ra and Pr (see Figs. 12, 13, and 14). We found that the data at constant Pr are consistent with $\mathrm{Nu}_{r,max}-1 \propto \mathrm{Ra}^{-0.35}$. The Pr de-

pendence at constant Ra could be given by $\mathrm{Nu}_{r,max}-1 \propto \mathrm{Pr}^{0.65}$, although the error of this exponent is about 50%. We found that the location $1/\mathrm{Ro}_{max}$ of $\mathrm{Nu}_{r,max}$ can be represented by the power law $1/\mathrm{Ro}_{max} \propto \mathrm{Pr}^{1.37}\cdot\mathrm{Ra}^{-0.18}$.

D. Concluding remarks

With our analysis we hope to provide sufficient data and a good starting point for theoretical modeling of rotating turbulent Rayleigh-Bénard convection in the buoyancy-dominated regime. Such modeling was already challenging for non-rotating convection where only two control parameters (Ra, Pr) are relevant [66–69]. It will be even more challenging for the rotating case where the parameter space is larger. However, the existence of the different $1/\mathrm{Ro}$-ranges suggests that only a few mechanisms have to be considered, and that in each range a different mechanism is dominating the changes of the heat transport with increasing rotation rate. We note that analyzing $1/\mathrm{Ro}_c$, S_{Ro}^+, $\mathrm{Nu}_{r,max} - 1$, and $1/\mathrm{Ro}_{max}$ provide quantitative independent information about several mechanisms. From $1/\mathrm{Ro}_c$ we learn under which conditions vortices form close to the top and bottom boundaries (as shown in Ref. [36]) while S_{Ro}^+ is indicative of the strength of Ekman pumping once vortices have formed. The relative strength of Ekman pumping and TP suppression determines the values of $\mathrm{Nu}_{r,max}-1$ and $1/\mathrm{Ro}_{max}$.

Qualitatively one sees that S_{Ro}^+ is essentially independent of Ra and depends only weakly on Pr, indicating that Ekman pumping is not strongly Ra and Pr dependent. On the other hand, $\mathrm{Nu}_{r,max} - 1$ and $1/\mathrm{Ro}_{max}$ show a stronger Pr and Ra dependence, indicating that the location and size of the maximal heat-transport enhancement are determined mostly by the Ra and Pr dependences of the heat-transport reduction in the bulk due to the TP effect. As $1/\mathrm{Ro}$ increases through ranges II and III, the heat is still transported efficiently across the boundaries by Ekman pumping, but the thermal resistance of the bulk increases. As a result significant vertical temperature gradients develop in the bulk. Since the significance of the thermal resistance in the bulk increases with increasing $1/\mathrm{Ro}$ and $1/\mathrm{Ek}$, and because $1/\mathrm{Ek} = 1/(2\mathrm{Ro})\sqrt{\mathrm{Ra}/\mathrm{Pr}}$, one would expect that at a given $1/\mathrm{Ro}$ the thermal resistance increases with Ra but decreases with Pr. That is why, for constant Pr, Nu_{max} is smaller at larger Ra and is reached already at smaller $1/\mathrm{Ro}$. On the other hand, for constant Ra and at larger Pr a larger $\mathrm{Nu}_{r,max}$ is found and is reached only at larger $1/\mathrm{Ro}$.

In this paper we focused on the initial heat-transport enhancement Nu_r with increasing $1/\mathrm{Ro}$ and the decrease of Nu_r for larger $1/\mathrm{Ro}$. We did not consider in detail the subranges I_a and I_b, and did not examine other subranges that occur for large Ra (see sec. V A 1 and ref. [39]). These subranges become obvious in $\mathrm{Nu}_r(1/\mathrm{Ro})$ only at

the largest Ra, but should be observable at smaller Ra by studies of internal flow structures.

Most likely transitions between structures of different symmetry in the turbulent bulk (such as for instance the replacement of Ekman vortices near the plates by Taylor columns penetrating the entire sample) and/or changes in the various boundary layers (thermal, Ekman, Stewardson) are responsible for the additional transitions above $1/Ro_c$. Clearly, further experimental and numerical studies are needed for a better understanding of this very rich system.

[1] M. Heimpel, J. Aurnou, and J. Wicht, Nature **438**, 193 (2005).

[2] D. H. Hathaway, Astrophys. Journal **760**, 84 (2012).

[3] G. Glatzmaier, R. Coe, L. Hongre, and P. Roberts, Nature(London) **401**, 885 (1999).

[4] L. P. Kadanoff, Phys. Today **54**, 34 (2001).

[5] G. Ahlers, Physics **2**, 74 (2009).

[6] G. Ahlers, S. Grossmann, and D. Lohse, Rev. Mod. Phys. **81**, 503 (2009).

[7] D. Lohse and K.-Q. Xia, Annu. Rev. Fluid Mech. **42**, 335 (2010).

[8] Chill, F. and Schumacher, J., Eur. Phys. J. E **35**, 58 (2012).

[9] R. Krishnamurti, J. Fluid Mech. **42**, 295 (1970).

[10] R. Krishnamurti, J. Fluid Mech. **42**, 309 (1970).

[11] R. Krishnamurti, J. Fluid Mech. **60**, 285 (1973).

[12] S. Grossmann and D. Lohse, Physics Letters A **173**, 58 (1993).

[13] J. Bosbach, S. Weiss, and G. Ahlers, Phys. Rev. Lett. **108**, 054501 supplement (2012).

[14] M. V. R. Malkus, Proc. R. Soc. London A **225**, 196 (1954).

[15] C. Priestley, Aust. J. Phys. **7**, 176 (1954).

[16] C. H. B. Priestley, *Turbulent transfer in the lower atmosphere* (U. Chicago Press, Chicago, 1959).

[17] E. A. Spiegel, Ann. Rev. Astron. Astrophys. **9**, 323 (1971).

[18] A. Tilgner, A. Belmonte, and A. Libchaber, Phys. Rev. E **47**, R2253 (1993).

[19] E. Brown and G. Ahlers, Europhys. Lett. **80**, 14001 (2007).

[20] G. Ahlers, E. Bodenschatz, D. Funfschilling, S. Grossmann, X. He, D. Lohse, R. J. A. M. Stevens, and R. Verzicco, Phys. Rev. Lett. **109**, 114501 (2012).

[21] G. Ahlers, E. Bodenschatz, and X. He, Journal of Fluid Mechanics **758**, 436 (2014).

[22] P. Wei and G. Ahlers, J. Fluid Mech. **758**, 809 (2014).

[23] R. Krishnamurti and L. N. Howard, Proc. Natl. Acad. Sci. **78**, 1981 (1981).

[24] E. Brown and G. Ahlers, Phys. Rev. Lett. **98**, 134501 (2007).

[25] E. Brown and G. Ahlers, Phys. Fluids **20**, 075101 (2008).

[26] R. J. Stevens, H. J. Clercx, and D. Lohse, Europ. J. Mech. B **40**, 41 (2013), Fascinating Fluid Mechanics: 100-Year Anniversary of the Institute of Aerodynamics, {RWTH} Aachen University.

[27] S. Chandrasekhar, Proc. R. Soc. Lond. A **217**, 306 (1953).

[28] S. Chandrasekhar, *Hydrodynamic and Hydromagnetic Stability* (Oxford University Press, Oxford, 1961).

[29] H. T. Rossby, J. Fluid Mech. **36**, 309 (1969).

[30] F. Zhong, R. Ecke, and V. Steinberg, J. Fluid Mech. **249**, 135 (1993).

[31] K. Julien, S. Legg, J. Mcwilliams, and J. Werne, J. Fluid Mech. **322**, 243 (1996).

[32] K. Bajaj, G. Ahlers, and W. Pesch, Phys. Rev. E **65**, 056309 (2002).

[33] Y. Liu and R. Ecke, Phys. Rev. E **80**, 036314 (2009).

[34] R. Stevens, J.-Q. Zhong, H. Clercx, G. Ahlers, and D. Lohse, Phys. Rev. Lett. **103**, 024503 (2009).

[35] R. J. A. M. Stevens, J. Overkamp, D. Lohse, and H. J. H. Clercx, Phys. Rev. E **84**, 056313 (2011).

[36] S. Weiss, R. J. A. M. Stevens, J.-Q. Zhong, H. J. H. Clercx, D. Lohse, and G. Ahlers, Phys. Rev. Lett. **105**, 224501 (2010).

[37] S. Weiss and G. Ahlers, J. Fluid Mech. **684**, 407 (2011).

[38] D. J. Tritton, *Physical Fluid Dynamics* (Oxford University Press, New York, 1988).

[39] P. Wei, S. Weiss, and G. Ahlers, Phys. Rev. Lett **114**, 114506 (2015).

[40] E. King, S. Stellmach, J. Noir, U. Hansen, and J. Aurnou, Nature **457**, 301 (2009).

[41] K. Julien, E. Knobloch, A. M. Rubio, and G. M. Vasil, Phys. Rev. Lett. **109**, 254503 (2012).

[42] K. Julien, A. Rubio, I. Grooms, and E. Knobloch, Geophysical & Astrophysical Fluid Dynamics **106**, 392 (2012).

[43] R. E. Ecke and J. J. Niemela, Phys. Rev. Lett. **113**, 114301 (2014).

[44] S. Stellmach, M. Lischper, K. Julien, G. Vasil, J. S. Cheng, A. Ribeiro, E. M. King, and J. M. Aurnou, Phys. Rev. Lett. **113**, 254501 (2014).

[45] P. Vorobieff and R. E. Ecke, J. Fluid Mech. **458**, 191 (2002).

[46] J.-Q. Zhong, R. Stevens, H. Clercx, R. Verzicco, D. Lohse, and G. Ahlers, Phys. Rev. Lett. **102**, 044502 (2009).

[47] J.-Q. Zhong and G. Ahlers, J. Fluid Mech. **665**, 300 (2010).

[48] S. Weiss and G. Ahlers, J. Fluid Mech. **688**, 461 (2011).

[49] R. P. J. Kunnen, H. J. H. Clercx, and B. J. Geurts, Europhys. Lett. **84**, 24001 (2008).

[50] R. P. J. Kunnen, Y. Corre, and H. J. H. Clercx, Europhys. Lett. **104**, 54002 (2013).

[51] R. Stevens, H. Clercx, and D. Lohse, Phys. Fluids **22**, 085103 (2010).

[52] R. Stevens, H. Clercx, and D. Lohse, New J. Phys. **12**, 075005 (2010).

[53] A. Oberbeck, Ann. Phys. Chem. **7**, 271 (1879).

[54] J. Boussinesq, *Theorie analytique de la chaleur, Vol. 2* (Gauthier-Villars, Paris, 1903).

[55] E. A. Spiegel and G. Veronis, Astrophys. J. **131**, 442 (1960).

[56] M. Assaf, L. Angheluta, and N. Goldenfeld, Phys. Rev. Lett. **109**, 074502 (2012).

[57] M. Assaf, L. Angheluta, and N. Goldenfeld, Phys. Rev. Lett. **107**, 044502 (2011).

[58] J.-Q. Zhong, D. Funfschilling, and G. Ahlers, Phys. Rev. Lett. **102**, 124501 (2009).

[59] S. Weiss and G. Ahlers, J. Fluid Mech. **676**, 5 (2011).

[60] G. Ahlers, Phys. Rev. E **63**, 015303 (2000).

[61] P. Roche, B. Castaing, B. Chabaud, B. Hebral, and J. Sommeria, Eur. Phys. J. **24**, 405 (2001).

[62] J. Niemela, S. Babuin, and K. Sreenivasan, J. Fluid Mech. **649**, 509 (2010).

[63] P. Oresta, G. Stingano, and R. Verzicco, Eur. J. Mech. B **26**, 1 (2007).

[64] G. Ahlers, M. C. Cross, P. C. Hohenberg, and S. Safran, J. Fluid Mech. **110**, 297 (1981).

[65] See Supplemental Material for fitted Parameters.

[66] S. Grossmann and D. Lohse, J. Fluid. Mech. **407**, 27 (2000).

[67] S. Grossmann and D. Lohse, Phys. Rev. Lett. **86**, 3316 (2001).

[68] S. Grossmann and D. Lohse, Phys. Fluids **23**, 045108 (2011).

[69] R. J. A. M. Stevens, E. P. van der Poel, S. Grossmann, and D. Lohse, Jour **730**, 295 (2013).